ALMA MATER STUDIORUM
UNIVERSITÀ DI BOLOGNA

MASTER II LIVELLO
SPACE MISSIONS SCIENCE, DESIGN AND APPLICATIONS
(SPICES)

- PROJECT WORK -

An Accessible Workflow for Selecting, Calibrating, and Testing Visible-Light Cameras for Non-Cooperative Satellite Detection in LEO

Supervisor: Alessandro Bevilacqua

Alfonso Cavallo

To those who are just starting a new journey,
full of sacrifice and fulfillment.

Contents

Abstract

In-orbit Space Situation Awareness (SSA) is a critical task for space-based assets. Being able to observe and understand the surroundings in real-time is necessary in order to avoid dangerous collisions or to perform rendezvous operations. This is particularly true in Low Earth Orbit (LEO), which is crowded with debris and potentially threatening non-cooperative spacecraft. Nowadays, with the increase of private and governmental actors in space, spacecraft security is rapidly becoming a critical need for both military and civil assets. This work introduces an investigation on state-of-the-art passive and active sensors for Resident Space Objects (RSO) detection. Its main contribution is a simple and accessible workflow for the requirements' engineering, calibration, and test of a space camera. The proposed workflow is implemented and validated, analysing the case study of an inexpensive commercial-off-the-shelf (COTS) device. The contribution provides the user with an accessible end-to-end guide to quantitative imaging for spaceborne SSA applications.

Chapter 1

Introduction

Protection from orbital threats is one, if not the single most important problem of today's orbital safety. Intensive mission launch and dangerous past civil and military experiments filled the Low Earth Orbit (LEO) with used rocket bodies, active and dead spacecraft, and orbital debris, many of which are travelling with huge amounts of kinetic energy, like space bullets. The task of monitoring such objects is called Space Situation Awareness (SSA). Today's approach is heavily based on collaborative tracking of Resident Space Objects' (RSOs) orbits stored in public and always up-to-date databases. However, most research has focused on the improvement of orbital debris tracking and cataloguing to predict and avoid collisions. However, due to the most recent geopolitical tensions, defence from potentially hostile spacecraft is gaining priority in national and international political agendas. This urge extends even to notoriously peaceful organisations like the European Space Agency (ESA), which is now seeking protection for its scientific assets from threats and countermeasures [1]. Despite trivial similarities, the space-to-space Detection, Recognition and Identification (DRI) of spacecraft comes with specific requirements, different from debris detection. While some constraints are relaxed, especially with respect to the higher visibility and size of the targets, dealing with a smart object performing unpredictable, sudden manoeuvres to avoid detection is the critical challenge. Debris trajectories are easily predictable with a degree of precision proportional to the surveillance capability; instead, hostile satellites may unpredictably and suddenly deviate from their path. The risk posed by other highly manoeuvrable spacecraft in modern warfare has already been addressed in the past [2], [3] under the name of Co-Orbital Anti-Satellite weapons (CO-ASAT) or space mines. Initially, those weapons were designed as kinetic weapons to crush against enemy assets, while today they are tasked with more sophisticated countermeasure activities. Such risk is ever-increasing with the improvement of thrust and on-edge autonomous decision-making. Smart orbital threats are now capable of Rendezvous and Proximity Operations (RPO). A smart CO-ASAT shall be considered capable of undergoing approach manoeuvres while minimising the chance of being detected, with the advantage of eclipse's darkness, dazzling sunlight, Earth's background, or other space environmental conditions adverse to sensors' detection. As a further factor, we are now living in the New Space Economy, where an increasing number of private actors, including defence companies, are following the fail-fast paradigm, prioritising inexpensive and rapid deployment over long-term mission design. This development paradigm further increases the amount of flying technology capable of RPO, both on the attacker and the defender size, increasing the demand for accessible SSA technology.

The goal of this work is to perform an investigation on the most used active and passive sensors for space-borne SSA in LEO orbit to provide information about the limits and the purpose of such technologies in a multi-sensor surveillance suite, provided scenarios with different types of approach. As an anticipation, among all the sensors, cameras are surely the most em-

ployed solutions for SSA. In addition, cameras are among the most developed and inexpensive devices, thanks to the cross-fertilisation from other consumer markets. For such reasons, a simple workflow is proposed to guide the definition of technological and optical specifications for an Electro-Optical (EO) camera satisfying performance requirements. Furthermore, a series of procedural steps is proposed for the radiometric and geometric calibration of the camera, and the characterisation and test of its detection performance. The entire pipeline has been designed to be highly affordable, as an easy entry point for any organisation willing to build or expand its business in the New Space Economy. To this aim, the case of a cost-effective Commercial-Off-The-Shelf (COTS) micro camera has been studied to validate the workflow, and as a demonstration that basic SSA capabilities can be achieved without the need for high-end assets. Despite the evident limit of the presented camera, similar technology has already flown up-to-date in commercial missions and experimented as an opportunistic sensor for the same purpose. As an example, D-Sense has been employed as a test bench for multiple on-board image processing studies [4], [5].

Structure of the Document

The document is organised as follows:

- **State Of The Art Analysis**: Chapter 2 describes the technology employed for Space Situation Awareness, with a focus on the most employed active and passive sensors and their role in a multi-sensor configuration;
- **Context and Visibility in LEO Orbit**: Chapter 3 provides details on the context and visibility in LEO orbit;
- **Proposed Workflow**: Chapter 4 provides a description of a proposed Workflow to support the choice of the camera and its requirement engineering, calibration, and testing;
- **Workflow Implementation**: Chapter 5 reports the implementation of the experimental workflow for a sample camera;
- **Workflow Validation**: Chapter 6 describes the validation of the results through a laboratory setup, serving as a simplified space analog;
- **Conclusion**: Chapter 7 concludes the thesis with a final discussion about the work, the results of the experiment, and future developments.

Chapter 2

State of the Art Analysis

Traditional SSA over debris is a necessary starting point to understand the optimal way to perform surveillance against non-cooperative satellites. Today, the localisation and cataloguing of RSO in orbit still leverages ground-based observatories distributed throughout the world, and involves the usage of advanced telescopes or high-power radars, both of which would not be feasible to deploy in orbit [6]. However, Ground-Based Space Surveillance (GBSS) comes with many limitations. Weather conditions and the dishomogeneous distribution of ground assets themselves deeply affect the detection performance, making it discontinuous and suboptimal. In this regard, Space-Based Space Surveillance (SBSS) is the most promising frontier of SSA improvement, proposing to monitor the orbit by means of a multi-sensor data fusion from constellations of spaceborne systems. Being deployed directly on the field, space sensors provide higher coverage, availability, and imaging performance, making integration between SBSS and GBSS the target for the future evolution of surveillance systems [7]. Focusing on onboard RSO detection, the most discussed passive sensors in literature are Electro Optical (EO) and Infra-Red (IR) Cameras, while the most popular active sensors are LiDARs and Radars. More specifically, much attention has been dedicated to optical surveillance constellations [7], [8], [9]. Many studies aim to exploit already space-proof and flying vision sensors for opportunistic detection, such as Star Trackers, ranging from detectability studies [10], [11] to detection algorithms [12], [13], or both [14]. Those sensors proved to achieve good detection capability even for sub-centimetre scale RSO. In the broader context of camera sensors, [15] performs an analysis of RSO LEO-to-LEO detectability by software simulation and diffuse sphere modelling for the debris. Simulation and testing of a space-based ESA optical telescope for statistical census of LEO debris is conducted in [16]. With regard to the employment of small satellites, [17] addresses the detection of non-cooperative targets through a collaborative system of nano-satellites around the International Space Station (ISS). A laboratory sensor calibration for cameras and a Star Tracker to improve RSO detection is introduced in [18]. Finally, [19] explores the feasibility of integrating AI-based image processing with vision sensors for LEO debris detection.

The previously introduced works all highlight the potential for visible light sensors. However, their application for non-cooperative active spacecraft is still limited, as is the amount of literature on the matter. EO cameras alone struggle with handling the detection in adverse environmental conditions as introduced in Chapter 1. In this regard, IR sensors are a good candidate for detecting eclipsed objects thanks to their ability to detect a satellite's IR emission and reflected Earth's IR emission, along with sunlight. Due to the onboard circuitry, spacecraft need to radiate internal heat for dissipation, with thermal emissions more dynamic than debris and natural rocks. However, most of the literature is focused on debris detection, indeed. In [20], the detectability of debris is put to the test through software simulation. Debris thermal signature characterisation

for enabling active removal is explored in [21]. In [22], the thermal IR characterisation of RSO is considered by means of a space telescope, along with the discrimination between debris and man-made objects. Nevertheless, IR cameras are still light sensors, and as such, they are easily saturated by IR beacons like the Earth and the Sun.

This marks the need for active sensors, like Radars and LIDARs, which do not rely on an emission or reflection from secondary sources to detect a target, but are capable of transmitting their own ranging signal. In [23], the application of both SAR and LIDAR has been explored, and encourages further investigation on LIDAR systems. An automotive LIDAR's employment for space-based space surveillance is proposed in [24], which also reports how poorly explored the application of such a sensor in modern SSA is. The concept of an Inverse Synthetic Aperture LIDAR has been investigated in [25], reporting the need for highly sophisticated coherence correction for distances farther than $100Km$ ranging. On the radar side, the design of a Sub-THz Inverse Synthetic Aperture Radar (ISAR) for SSA is proposed in [26], with centimetre resolution hundreds of kilometres, at the cost of restrictive technological requirements. In all the cases, two main limitations stand out for both LIDARs and Radars. The first constraint is the need for high-end technology and calibration required for achieving good enough performance to compete with passive sensors. The second constraint is the high power budget required by those systems, which is often hard to satisfy on edge for space platforms. Still, both those sensors overcome the limitations of passive ones in terms of availability and resilience, and are capable of observation even in unfavourable exposures. Recent research is also starting to address innovative sensors like event-based cameras, which are standing out as an excellent trade-off between power budget and performance [27], [28].

In summary, due to the individual limitations of each sensor, the need for a heterogeneous multi-sensor suite has emerged, as by Jena-Optronik GmbH in [29], particularly in the context of threat detection. The present research confirms the need for a multi-sensor suite capable of optimal allocation, such that each sensing system is able to make up for the limitations of the others. At the same time, it has emerged that among all the aforementioned sensors, visible cameras are surely one indispensable asset. They have the biggest Field of View (FOV), and the highest precision and reliability in detection, thanks to the advanced development achieved in the other consumer markets and the huge literature in the matter of image processing, even in SSA. Today, all those advantages make cameras the simplest, cost-effective and best-performing sensor for the task. Nevertheless, a visual confirmation is trivially always desired by human operators as a final confirmation. Many have analysed the observation capabilities of space cameras, for SSA and other fields such as vision-based RPO, either formally [10], [11], through simulation software [15], [30], in highly photorealistic laboratories [31], [32], or directly in orbit. Furthermore, a huge literature is available for both image processing and specific target detection, recognition, identification, and tracking. Still, to the best of the author's knowledge, the problem of designing a simple workflow integrating all the aforementioned steps into one unified procedure was never addressed. The purpose of this work is to provide the reader with an end-to-end step-by-step workflow, hereafter referred to as the *workflow*, for achieving an initial accessible visual SSA capability, from the estimation of camera requirements and theoretical performance, up to the digital calibration, characterisation, and the final test of the asset.

Chapter 3

Context and Visibility in LEO Orbit

Selecting and calibrating an appropriate camera is a procedural process that requires awareness of the LEO scenario and the desired detection conditions. In particular, the surveillance against incoming space threats depends on several variables and four main actors: the Sun, the Earth, the detecting satellite, hereafter referred to as Ego Satellite, and the target approaching satellite, hereafter referred to as Target Satellite. The *first factor* is the position of the Target with respect to the Earth's shadow:

- **Target in Eclipse**: the target lies in the Earth's shadow, not reflecting any light, hence it is completely invisible to an EO camera;
- **Target in Daylight**: the target is exposed to sunlight, and its reflection can be detected;

An object in LEO travels at $\sim 7.8km/s$ with two alternate phases, the Eclipse and the Daylight, both of them lasting ~ 45 minutes each. It is clear that the surveillance from the EO camera is effective only for half of the entire orbit, which is a severe yet unavoidable limitation.

The *second factor* is the position of the Earth with respect to the camera's boresight:

- **Earth in the Background**: the target lies between the Earth and the Ego satellite. The Earth's surface is not an ideal background as its reflection decreases the Signal-to-Noise Ratio (SNR), and may even blind the sensor, depending on the exposure or the presence of highly reflecting clouds;
- **Earth outside the Background**: the Earth's surface is not behind the target, which achieves peak visibility against the black of the void;

Taking into account a rotation axis centred in the Ego satellite and normal to the orbital plane, Earth covers $\sim 40\%$ of the $360°$ FOV around the satellite, creating a permanent region toward which the detection is degraded.

The *third factor* is the position of the sun with respect to the camera's boresight, which deeply affects the illumination, thus the detectability of the target:

- **Sun on the background**: the sun lies in the camera's FOV, saturating the sensor, potentially blinding and severely compromising the visibility in absence of proper countermeasures;
- **Sun outside the background**: the sun lies outside of the camera's FOV, and the detectability of the target depends on the amount of light reflected, hence the incident angle of the sunlight over the satellite's surface.

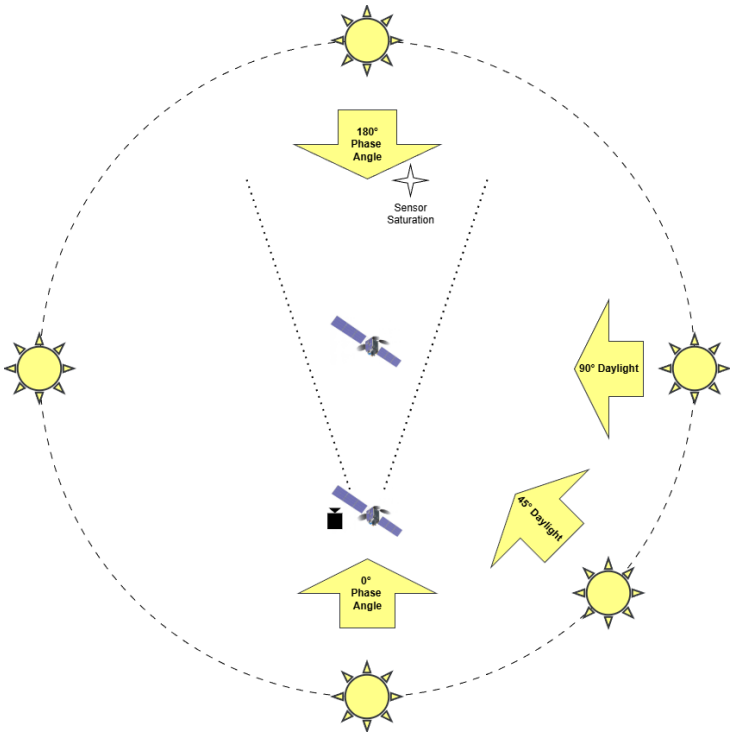

Figure 3.1: Possible Geometric Configurations of the Sun around the Ego–Target Satellite binary system.

Depending on the requirements, it can be worth addressing additional hard-to-model and lens-dependent undesired effects that may be introduced by the sunlight incident on the optic angles i.e. lens flares. A professional system provided with a mechanical filter can avoid those effects.

Figure 3.1 and Figure 3.2 summarise all the possible geometric configurations between the Sun and the Earth in daylight as relatively rotating around the Ego–Target satellite binary systems. Figure 3.1 focuses on the impact of the sunlight incident on the scene, highlighting the saturation occurring at $\sim 180°$. Figure 3.2, instead, comes into play when the system Ego–Target satellite is considered rotating around an axis normal to a plane intersecting the Earth, highlighting the negative impact of the Earth's background on the detection. As a confirmation of what is reported in the previous Chapters, the camera alone is a very limited sensor, but it is also the most cost-effective and best performing under favourable light conditions.

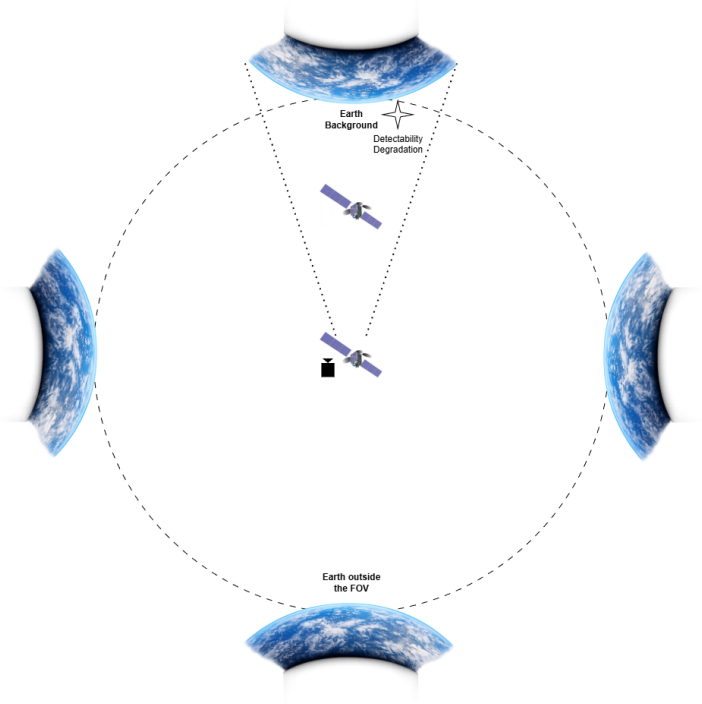

Figure 3.2: Possible Geometric Configurations of the Earth around the system Ego–Target Satellite (on a plane intersecting the Earth).

Chapter 4

Proposed Workflow

A technical procedure shall inform the end-to-end camera engineering, from selection to test and deployment. This section introduces all the theoretical steps for the proposed *Workflow*, illustrated by Figure 4.1 and summarised by the following sequence:

1. **Detection Performance Formal Estimation**: during this step, a candidate camera is selected, and a set of formal computations is proposed to estimate the approximate detectability of the RSO with respect to a given EO camera sensor and optic specifications. The objects are modelled as Lambertian spheres;
2. **Geometric Calibration**: once the selected camera has been confirmed, it shall be calibrated to correct unwanted effects derived from the camera's optical properties, which may lead to mistaken spatial estimations during the targets' positioning and tracking;
3. **Radiometric Calibration**: the selected camera shall undergo a radiometric calibration process to ensure the intensity of the pixel is proportional to the actual light intensity, such that the measures can be employed for radiometric estimation, as a radiometer, indeed;
4. **Noise Characterisation**: the noise affecting the sensor shall be estimated at all the intensity values, to increase the detection confidence against possible false positives and to better verify the achievable detection performance;
5. **Resolution Characterisation**: once the estimated resolution has been verified, more in-depth tests shall be performed to understand how the light projected onto a sensor's pixel is spread across neighbouring pixels, to achieve a more reliable measure of the actual spatial resolution of the camera;
6. **Detection Performance Testing**: the camera detection performance shall be tested in a laboratory environment before the deployment.

4.1 Experimental Resources

The proposed *workflow* requires a set of affordable materials and instrumentation. Each of such resources is illustrated by Figure 4.1, associated with the steps in which it comes into play. It follows a descriptive list of devices:

- **Calibration Chessboard**: a chessboard with well-known edge size or any pattern precisely measured and carefully stretched out over a flat surface [33] to avoid unwanted errors from small imperfections;

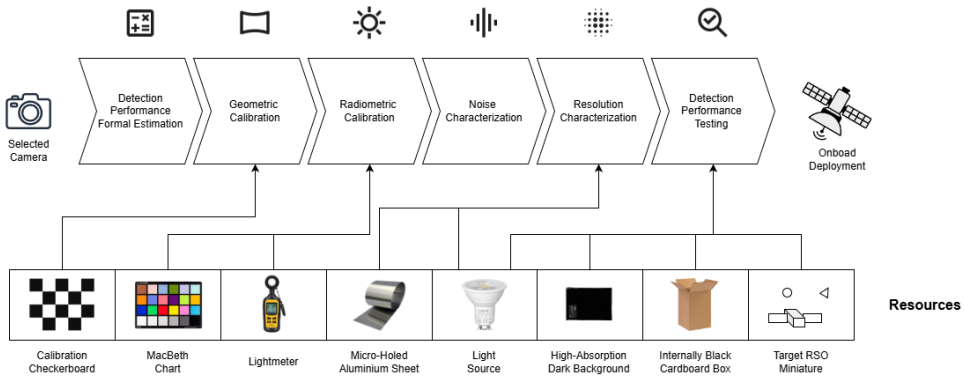

Figure 4.1: End-to-End Camera Requirement Engineering, Calibration, and Testing Workflow.

- **Macbeth Chart**: a board of patches, each of which is uniform in properties and with well-known colour and reflectivity. It is usually employed for colour calibration in commercial cameras, but can be employed to test the reliability of radiometric measures. Specifications about the patches are reported in [34];
- **Light Meter**: a simple measurement instrument that is able to measure the light flux incident on the detector's surface, typically in lux;
- **Aluminium Sheet**: easily accessible, even kitchen aluminium can be used. It can be micro-holed with a needle and backed by an LED or steady torch light for Point Spread Function (PSF) characterisation. Any thin, fully opaque material in which a circular aperture may be made is employable;
- **Light Source**: A light source with a spectrum as close as possible to the natural sunlight, optionally dimmerable. Trivially, this needs to be used to simulate the incident sunlight in the LEO orbit simulation test. For a high-end setup, it is possible to go after realistic exposure through professional spotlights, with uniform directional beams, the actual spectrum, and incident flux as the real sunlight. More accessible alternatives may still rely on narrow-beam house LED lights and aim to validate the detection in multiple fainter light conditions, taking advantage of dimmers and intensity filters. If the main concern is to avoid scattering, a collimated laser can be employed instead;
- **A Dark Room**: a clean, optically insulated, and closed dark space to simulate the darkness of the void; Ideally, a dedicated actual *dark room* with absorbent walls is desired, as used in many orbital optical simulations. However, a Cardboard Box can be used in place of it with proper adjustments. In that case, the box material shall be fully opaque, and the internal walls as black in the visible light range as possible;
- **Target 3D/2D Miniature**: scaled RSO miniatures of expected detection targets to shoot photos at during testing, ideally tridimensional. For instance, those can be easily produced through a 3D printer and painted with paint recalling the reflection properties of the actual expected materials. Due to the accessibility of such an asset, the required model size is usually conditioned by the choice of the *dark room*. In particular, when using small cardboard boxes or similar surrogates, a micro-metre-scaled photo target may be required, making it hard to find suitable assets. In this case, it is possible to rely on approximated models such as industrial microspheres, usually used for microscope calibration, or accept a partial loss in reflection realism and fold back to more house-made solutions such as corianders, glitter, or paper cut-outs;
- **Dark Background**: A professional low-reflectance background surface. It is usually not trivial to set up an ideal *dark room* entirely covered by fully absorbent inner walls. It is

easier to look for common black tints or materials that minimise the amount of bouncing light just enough. What is really critical is the absorptivity of the background. In this regard, it is recommended to equip with a highly-absorbent black sheet, material, or paint that is able to retain more than 99% of the incident visible light, and to achieve as much coverage as possible of the background in the camera's FOV. Materials like that are nowadays inexpensive, easy-to-find consumer products for photography and artistic expositions.

Finally, a pool of candidate cameras shall be selected for validation, calibration, and testing, for example, among COTS products within the budget. The *workflow* shall help the engineer estimate their performance before the purchase, and calibrating and testing one or multiple sensors once acquired.

4.2 Step 1: Detection Performance Formal Estimation

The employment of Star Trackers as opportunistic sensors for improving the SSA has been widely explored in recent years. For such a reason, RSO visibility in space has mostly been explored by means of measurement standards familiar to the field of star observation and tracking. In this regard, [10] provides the reader with a comprehensive set of relevant camera properties and relative formal estimation, which this section is going to summarise. Such estimation shall support the engineer in deciding whether one camera is feasible according to the minimum detection requirement defined for the project.

4.2.1 Detectability

Any object appears at a camera with an intensity called an Apparent Visual Magnitude (AVM), which is a logarithmic function of the incident flux. In the same way, the AVM of a target satellite m_{rso} modelled as a Lambertian sphere can be estimated as a function of the Sun's AVM, its incidence angle over the exposed surface, and the reflectivity of its material reported in Equation 4.1.

$$m_{rso} = m_{sun} - 2.5 \log_{10} \frac{A_{\text{opt}}}{R^2} \tag{4.1}$$

where $m_{sun} \approx -26.5$ is the AVM of the sun at LEO; R is the distance; A_{opt} is the optical cross-section, which is a measure of how much light the object reflects. In turn, it can be computed through 4.2.

$$A_{\text{opt}} = \frac{1}{4}\pi d^2 \rho F(\phi) \tag{4.2}$$

where d is the diameter of the object's equivalent Lambertian sphere; ρ is the reflectivity of the satellite's surface material; F is the phase function, a measure of how much light is reflected with respect to the angle ϕ between the Ego–Target vector and the Sun–Target vector. $F(\phi)$ is defined by Equation 4.3

$$F(\phi) = \frac{2}{3\pi^2}[(\pi - \phi)\cos(\phi) + \sin(\phi)] \rightarrow F(0) = \frac{2}{3\pi} \tag{4.3}$$

The detection capability of a Star Tracker, hence of a camera, can be measured in terms of a Magnitude Limit m_{lim}, also referred to as Apparent Visual Magnitude (AVM) cutoff. Many Star Tracker datasheets provide such information, while it may be harder to retrieve for traditional cameras. In this regard, [35], which studies the accuracy of Star Trackers, provides the reader

with a set of useful equations. As a premise, let us consider the worst-case scenario, where the illuminated area of the target has a sub-pixel theoretical projection onto one single pixel. In such a case, the accumulated light flux will be spread over neighbouring pixels by the PSF, on a Region Of Interest (ROI) that we model for simplicity as a $k \times k$ square.

With this in mind, the limiting incident flux F_{lim} on the camera, measured in photons, can be computed as the quantity that achieves a minimum reference SNR for given noise values:

$$F_{\text{lim}} = \text{SNR}^2 \frac{1 + \sqrt{1 + 4k^2(\sigma_{\text{rd}}^2 + N_{\text{bg}}\tau)\text{SNR}^{-2}}}{2\tau Q_{\text{opt}} Q_{\text{eff}}} \tag{4.4}$$

where SNR is the minimum reference Signal-to-Noise Ratio; σ_{rd}^2 is the readout error; N_{bg} is the background noise, which in space is mostly addressable to the dark signal; τ is the exposure duration; Q_{opt} is the transmission coefficient; Q_{eff} is the quantum efficiency of the device. Hardly available information like the camera's efficiency and the noise levels can be both approximated with reference values, obtained for similar scenarios and devices, or assumed ideal $(Q_{\text{eff}} = Q_{\text{opt}} = 1; \sigma_{\text{rd}}^2 = \sigma_{\text{bg}} = 0)$, keeping in mind that the measure is affected by a relevant approximation error. As for k, instead, $k \in \{2, 3, 4, 5\}$ is a good approximated value set where larger values assume a higher degradation of the signal.

Once F_{lim} is computed, m_{lim} is retrievable through the following equation, which can be applied to convert any flux to a magnitude:

$$m_{\text{lim}} = -2.5 \log_{10} \frac{4F_{\text{lim}}}{\pi D^2 f_{m=0}} \tag{4.5}$$

where D is the aperture diameter; $f_{m=0}$ is the bolometric zero points, which is generally recognised as Vega's flux at the Earth $f_{vega} = 2.51802 \times 10^{-8} \frac{W}{m^2}$. An RSO can be detected if its $m_{rso} \leq m_{\text{lim}}$.

4.2.2 Angular and Spatial Resolution

Optical sensors and Star Tracker's ability to distinguish two close objects as different is called spatial resolution. More specifically, the Angular Resolution is the minimum angle between the first object, the detector, and the third object at which it is possible to distinguish the two targets as distinct. A camera's angular resolution can be governed by one of two phenomena, the diffraction limit and the detector limit.

A camera is diffraction-limited, where its spatial resolving capability is constrained by the physical phenomenon of diffraction, which causes light to bend while passing through an opening such as the aperture of the camera. The angular resolution can be estimated with Equation 4.6.

$$\theta_R = \arcsin\left(1.2197 \frac{\lambda}{D}\right) \tag{4.6}$$

where λ is the light wavelength, and D is the diameter of the lens. Such angular resolution can be converted into a Projected Space Resolution Distance (PSRD), which is the minimum linear distance on the object plane where two different objects may be distinguished. As such, it is dependent on the distance from the object plane R, and can be estimated as in Equation 4.7.

$$PSRD_R \approx R \cdot \theta_R \tag{4.7}$$

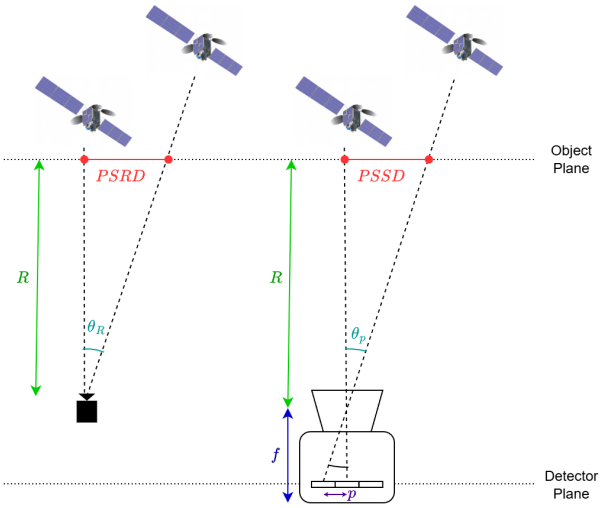

Figure 4.2: Geometric Definition of diffraction-limited θ_R and detector-limited θ_P angular resolution and projected linear resolutions.

More often, a space camera is detector-limited, meaning it is constrained by the FOV of its pixels. The detector's limited angular resolution can be estimated with Equation 4.8.

$$\theta_p \approx \arctan\left(\frac{p}{f}\right) \tag{4.8}$$

where p is the pixel's edge size over one considered dimension, horizontal or vertical with respect to the image plane; f is the focal length. As for the diffraction-limited angular resolution, this property can be converted into a linear metric on the object plane, called Projected Space Sample Distance (PSSD), estimable through Equation 4.9.

$$PSSD_R = R \cdot \theta_p \tag{4.9}$$

Ground-based cameras are also affected by atmospheric factors, which can be ignored in space. Additionally, the assumption of the lack of optical aberration and other imperfections of the lens can be made to simplify the estimations. Figure 4.2 illustrates the geometric definition of the angular and linear resolution of the camera for both the diffraction-limited and detector-limited scenarios.

4.2.3 Streak Speed

Most satellites, especially the ones lying in a different orbital plane, do not travel aligned with the Ego satellite. The relative movement of the Target satellite on the object plane can cause the object to appear as a line in the image, rather than a point. The less aligned the direction of the two satellites, the higher the orthogonal velocity component, which streaks over the plane, and the longer the line. For exposures $\tau \leq 0.1$, such a line can be approximated as a straight line. Through formal computation, it is possible to derive the object's streak speed by analysing the length of this line d, in particular on the object plane $S = \frac{d}{\tau}$. However, if the streak line is not fully included in the image, in particular when both endpoints are outside of the frame, nothing can be said. With this in mind, the maximum detectable streak speed S_{max} is, indeed, conditioned on the camera's FOV and such a relation is expressed in Equation 4.10.

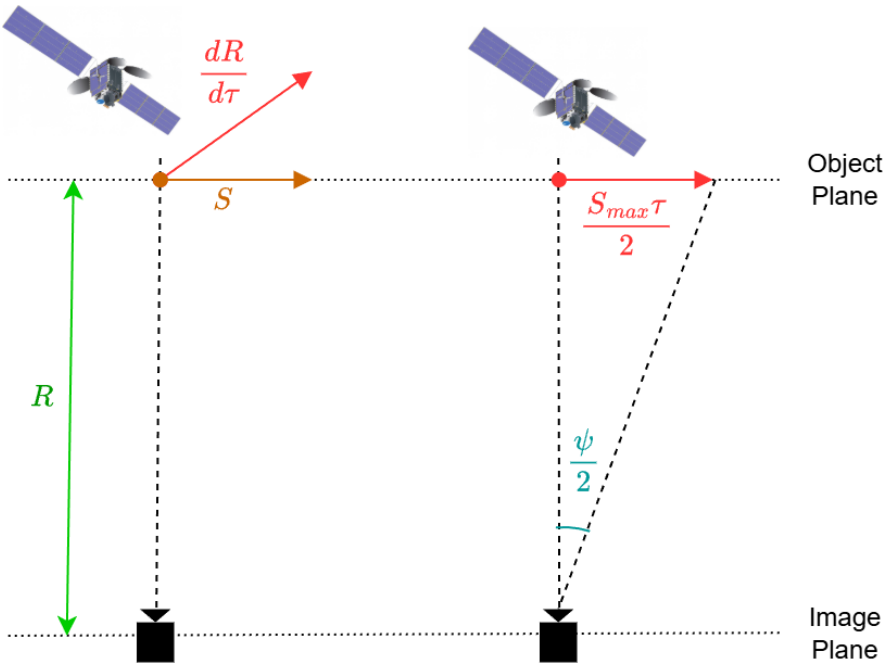

Figure 4.3: Geometric Definition of the Streak Speed and the Maximum Streak Speed.

$$S_{max} = \left[\frac{2\tan(\frac{\psi}{2})}{\tau}\right] R \tag{4.10}$$

where ψ is the square FOV; R is the distance from the camera; τ is the exposure. An $S > S_{max}$ would cause the object to describe a line too long to be contained inside a frame. A geometric definition of the maximum streak speed is illustrated by Figure 4.3.

4.3 Step 2: Geometric Calibration

All cameras leave production with non-ideal camera characteristics and lens imperfections. Camera's characteristics affect the projection model, while lens' effects introduce radial and tangential distortions. In fact, the image capture process is the projection of a 3D point into the 2D image plane of the detector, and can be modelled through the relation in Equation 4.11.

$$k\bar{m} = \mathbf{P}\bar{M} = \mathbf{KB}\bar{M} \tag{4.11}$$

where $\bar{M} = [X, Y, Z, 1]^T$ is a 3D point in homogeneous coordinates; $\bar{m} = [u, v, 1]^T$ is the projected 2D homogeneous coordinates on the image plane; k is the homogeneous scaling factor; **P** is called a projection matrix. The factors which define the projection are the intrinsic matrix **K** and the pose **B**. **K** represents the scale and offset operations conditioned on the camera's geometry, while **B** defines the pose (rotation and translation) of the point in the camera's reference frame. Equation 4.12 defines the intrinsic matrix in more detail.

$$\mathbf{K} = \begin{bmatrix} f_x & s & c_x \\ 0 & f_y & c_y \\ 0 & 0 & 1 \end{bmatrix} \in \mathbb{R}^{3\times 3} \tag{4.12}$$

where f_x, f_y are the focal lengths in pixels; s is the shearing between the axes ($s \neq 0$ implies they are not orthogonal); c_x, c_y represent an offset in the projections over the image plane, with respect to the centre. Equation 4.13 defines the pose matrix.

$$\mathbf{B} = \left[\mathbf{R}|t\right] \in \mathbb{R}^{3\times4} \tag{4.13}$$

where $R_{3\times3}$ applies a rotation to align the 3D point with the reference orientation and $t_{3\times1}$ applies a translation according to the new reference centre. While the pose dynamically changes in different pictures according to the actual position of the point in space, the intrinsic matrix is fixed and depends on the aforementioned camera characteristics; it can be normalised. To fix the projection, it is necessary to compute the inverse $\mathbf{K}^{-1}$ of $\mathbf{K}$, which implies that $\mathbf{K}$ must be measured.

The scope of the geometric calibration is to find the intrinsic matrix and the pose matrix. In [36], a simple technique is proposed to compute them by means of an homography with a known pattern stretched over a flat plane assumed with ($Z = 0$). A chessboard with a well-known edge size is usually employed, but other patterns can be adopted. Such patterns are easily retrievable online under the keyword "calibration checkerboard/chessboard". The procedure, described in mathematical details in the cited paper, requires at least two pictures of the pattern taken with the camera that needs to be calibrated, at two different orientations and positions. The computation is based on the closed-form solution of a set of linear geometrical equations and a maximum-likelihood non-linear optimisation. The `python/C++ OpenCV` library provides a ready-to-use implementation and several tutorials on such an algorithm [37], that will also perform sub-pixel refinements on the detected pattern's position, necessary to achieve better results. Furthermore, it will provide distortion coefficients, useful for correcting tangential and radial distortions.

The following recommendations are provided to the reader:

- Take at least 20 photos to achieve more accurate results. While the algorithm requirement is just two, the results should be more accurate and reliable with multiple diversified samples;
- Care for taking pictures where the pattern is well-illuminated, in focus, still, entirely contained in the frame, and turned toward the camera;
- Care for taking multiple pictures of the pattern in different regions of the frame (up, down, corners, etc.) to maximise the coverage and ensure any distortion in any part of the image is accounted;
- Care for taking multiple pictures of the pattern at different challenging orientations and distances to improve the result.

Figure 4.4 reports an example of a photo of a chessboard pattern used for calibration, along with the detection markers of the squares' vertices, that is to say, the projected pattern's points. Once the calibration is performed, it is strongly recommended to perform a re-projection of the pattern's 3D point into 2D image coordinates. It consists of picking each point of the pattern from a list respecting the pattern's well-known geometrical constraints, and re-projecting them onto the image plane through the intrinsic and pose matrices estimated with the calibration algorithm for a reference image. Once the 2D coordinates have been obtained, it is easy to compute the error with respect to the actual 2D coordinates of the point detected on the reference image in terms of pixel distance. This metric will provide the reader with an estimate of how prone one point is to being projected onto the wrong pixel, and how far. Average errors < 0.3 are generally good, while values > 0.5 imply a chance for the point to be projected on an adjacent pixel rather than the expected one. One can expect the distribution of the error, where the mean error for

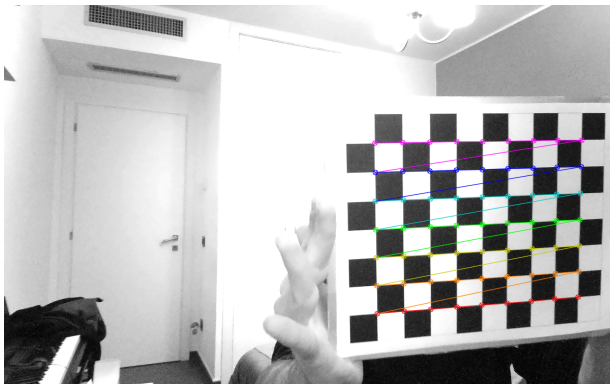

Figure 4.4: Example of a picture of a Calibration Chessboard for Intrinsic and Pose matrices estimations.

each image is a sample, to be a couple of Gaussian bells, one main denser distribution, and a second curve centred at higher error values. This second curve refers to more challenging conditions, like extreme orientations or pictures taken at corners of the frame. Should this second peak be far enough from the main one and much less dense, it is recommended to exclude such too-extreme outliers from the computation.

In conclusion, once this geometric calibration procedure is concluded, the estimated intrinsic matrix can be inverted and used to correct the projection error. Also, distortion parameters can be used to remove non-linear effects. For the next calibration steps, it is now always required to perform this geometric inversion and undistortion first, before proceeding with further processing and analysis.

4.4 Step 3: Radiometric Calibration

A camera sensor always has an internal raw image, in which each pixel's intensity is a direct measure of the quantity of received light, that is to say, the intensity of a light source. However, most COTS cameras are not designed for industrial applications, but rather focus on providing the consumer with the most pleasant image in terms of visual perception. To this aim, those sensors rely on Image Signal Processing (ISP) pipelines, chains of operations that manipulate the raw image into the desired result. Those operations include both linear and non-linear transformations like colour correction, contrast enhancement, gamma correction, white balance, etc. The ISP can change both colours and intensity values in the raw input, making them not reliable anymore for radiometric measurements. If possible, it is always strongly suggested to retrieve the raw image rather than some processed output.

Nonetheless, the raw image itself may be affected by non-linearities that are wavelength-dependent and attributable to a peculiar response of the specific detector. In order to be able to infer properties about the target based on its intensity, it is necessary to obtain an image format where the pixel value is a reliably linear function of the actual flux. Now, let us call the concatenation of the sensor's response and the ISP chain a Camera Response Function (CRF). Let us model the CRF over a raw image I_{raw} as a pixel-wise function f_{ISP}, such that the final output image $I(x, y) = f_{\text{ISP}}(I_{raw}(x, y))$, for all pixels with image coordinate (x, y).

As aforementioned, it is necessary to revert to a raw representation to enable the use of the sensor as a radiometer. It is required to find the inverse function $g = f_{\text{ISP}}^{-1}$, such that applying this function to the output image, we can revert to the original raw image as $I_{raw}(x, y) = g(I(x, y))$. A calibration procedure to obtain g is proposed by [38], also known as Debevec algorithm. This procedure requires taking at least two photos, I_1 and I_2, of the exact same scene under the

same illumination, with two arbitrary well-known exposures τ_1 and τ_2, respectively. The method exploits the property by which the amount of flux measured by the pixel as intensity $I(x, y)$ is directly proportional to both the exposure τ and the actual flux incident the pixel $E(x, y)$ as $I(x, y) = E(x, y) \cdot \tau$. Trivially, the more the duration of the exposure, the more the accumulated photons.

In the Debevec algorithm, g is modelled as a radiance map that associates each intensity value $k \in \{0, 1, 2, ..., 255\}$ with a new value in the same discrete range, optimised to maximise the linearity with the exposure times. It is also possible to tune a regularisation hyper-parameter to soft-constrain the smoothness of g over the discrete range $[0, 255]$. It is worth noting that by its very nature, a CRF shall be a monotonically increasing curve, and the optimisation shall be tuned to achieve such a result. This method is non-parametric, flexible, simple, and works well with very discontinuous CRF, provided the accurate exposure times.

On the other side, in the presence of a more linear CRF, and where approximated ratios between the exposures are available rather than the absolute values, other methods can be more suited to the problem. An alternative parametric approach is presented in [39], which is based on fitting a polynomial CRF model, minimising the error between the ground-truth exposure ratios and the ones retrieved after applying the model. Despite its effectiveness, this method may easily converge to ill-posed non-monotonic curves in the presence of highly non-linear behaviours in the input images' ratios.

In either cases, it is suggested to use a Macbeth Chart has a photographic target. Macbeth Chart's patches have the useful properties of being uniformly reflective and having well-known reflectivity coefficients that can be retrieved from [34]. Not only does it make it possible to cover a heterogeneous pixel intensity value range, but it also makes it possible to verify that the intensity values are proportional to the reflectivity coefficients of the patches, adding a further test layer other than linearity with the exposure values.

Once the photo have been acquired at different exposures, the algorithm ran, and the linearity of the inverted pixel values with the exposures and patch reflectances verified, we can obtain an image where pixel values are proportional to the actual perceived incident flux. Still, the pixel value does not measure the actual flux F. We have to obtain a gain G such that $F = I_{raw}(x, y) \cdot G$. Let us simply measure, through the use of a Radiometer, the amount of Lux F_{patch} incident over a non-saturated patch with pixel values $I_{patch} < 255$. At this point $G = \frac{F_{patch}}{I_{patch}}$. The property of the sensor to saturate at 255 for the same flux at any exposure is another law that can be exploited to get an absolute reference. In the end, a radiometer will always be required in calibration to enable the use of the camera as a radiometer itself.

In conclusion, this CRF inversion procedure shall now always be applied as a second step after the geometric correction to obtain linear raw images. Whether the user needs to measure the real flux from a given instantaneous FOV (IFOV), it is just necessary to multiply a non-saturating intensity on the retrieved raw image by the gain G.

4.5 Step 4: Noise Characterisation

All the cameras are affected by noise. Pixel values are unreliable due to the presence of unwanted, often random contributions, with different sources and statistical patterns. While some of the causes are rooted in the circuitry and processing, others are physical phenomena, mostly based on the discrete nature of the photons and the temperature. In either case, it is widely accepted in the literature that such a noise is related to the measured pixel's intensity. In order to measure the sensor's noise, let us perform the calibration at a temperature we consider the

worst-case scenario with respect to the expected ranges in orbit. A minimum thermal control is always suggested, as $\geq 120°C$ values can be easily reached in LEO.

A simple self-calibration noise method is proposed in [40], through non-parametric modelling. The method requires capturing a video of a still scene with unchanging illumination, possibly achieving an as-extensive-as-possible coverage of the entire pixel intensity range $[0, 255]$. In other words, too dark, too bright, or too uniformly coloured scenes have to be avoided. In summary, the algorithm processes the video as a sequence of supposedly identical frames and works as follows:

1. The sequence of frames is split into two subsequent halves I_1 and I_2;
2. The median is computed over all the pixels across all the frames in I_1;
3. For each pixel, its shift in intensity from the median computed over I_1 is measured for each frame in I_2. Whether a pixel shifts too much (shift greater than a given threshold) in too many frames (count greater than a given threshold), the entire pixel is discarded as an outlier for all the computations;
4. The mean across all the frames in I_2 is computed, and that value is considered the reference value of the pixel. Any shift from the mean for each frame is considered an error;
5. All the errors are computed and counted for all the frames in I_2, and the distribution is plotted as a histogram.

Ideally, each of the intensity values $\{0, 1, ..., 255\}$ should be the mean for at least one reliable pixel, and the noise distribution should be somehow continuous, with higher noise on higher values. However, it is not rare that an extremely non-linear ISP squashes some values, causing some of them to be rounded and disappear. Such "lost" intensity values do not appear even after the inversion of the CRF. Furthermore, new intensity values may appear as a consequence of the spatial interpolations caused by the geometric correction, with less reliable noise distributions. A more discontinuous behaviour in the noise distributions is not unexpected when dealing with the correction of highly non-linear images.

Finally, one can simply capture a video with the lens cap on and compute the mean intensity value across all the frames and pixels to be used as a baseline noise level for space photos in LEO. However, it is also recommended to analyse each pixel, should some of them be exposed to specific defects and report higher noise values.

4.6 Step 5: Resolution Characterisation

Section 4.2 explained how to derive the linear resolution of a detector. The computation shall be verified by photographing a well-centred meter or any object with a well-known reference length at a given distance, and measuring whether one pixel covers exactly the expected amount of space. Once the linear resolution has been verified, deriving the apparent area projected by an object onto the detector plane is another trivial linear computation problem. However, even in cases where such a projection is sub-pixel, the intensity on an ideal point is always spread across multiple neighbouring pixels as an airy disk. This is due to multiple causes such as diffraction, de-focus, optical aberrations, etc. Such phenomena can all together be modelled as one convolutional kernel function called the Point Spread Function (PSF).

The size of the disk projected by an ideal point defines the actual spatial resolution of the sensor and needs to be estimated. Furthermore, it is expected to have a worsening and a stretch of such an effect on the margins of the images, making it necessary to measure the PSF

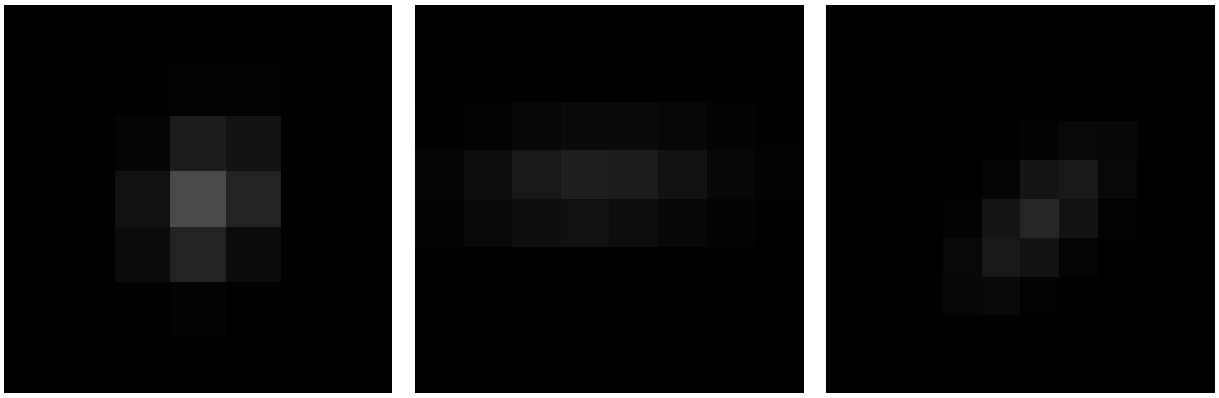

(a) (b) (c)

Figure 4.5: Discretised Point Spread Function at: the centre (a), the left corner of the frame (b), the down-left angle of the frame (c).

at different corners of the frame. Figure 4.5 shows some examples of PSF in different frame regions.

The simplest way to estimate the PSF is by means of an almost-ideal point light, which can be approximated with a small retro-illuminated hole in a fully opaque material, like an aluminium sheet. The procedure is described in the following sequence of steps:

1. Use a needle or a very thin spiky object to perform a rounded micro-metric hole in the aluminium. Take care to keep the aperture as circular as possible by rotating the spike, and free from obstructions by removing the remaining metal strips with the help of tweezers or other tools;
2. Place a well-centred light source behind the aperture;
3. Place the retro-illuminated sheet on a plane perpendicular to the camera boresight, at a distance where the hole is in focus and projects as an ideal point in perspective;
4. Ensure that the light brightness is not saturating the sensor, otherwise the measurement is not reliable;
5. Take nine photos, where the PSF is located approximately at the marks illustrated by Figure 4.6, so as to cover all the main regions of the frame.

Once the pictures are taken, and the photos processed through the previous correction algorithms, the PSF shall appear as a pixelled ellipsoid, typically in a rectangle with up to 5 pixels per edge. The size and orientation of the major semi-axis of the ellipsoid shall depend on the location of the PSF in the frame. Larger stretches can be expected at the corners, and larger inclinations can also be expected at the angles.

A PSF can be modelled as a normal multi-variate Gaussian distribution $\mathcal{N}(\bar{\mu}, \Sigma)$ over two axes x and y, where Σ non-diagonal values encode an inclination $\theta \in [-45°, 45°]$ around the normal to the image plane. To obtain a quantitative estimate of the PSF parameters from the image, let us fit the parametric model through a maximum-likelihood optimisation algorithm. Once the Gaussian bell has been fitted over the PSF image, the Full-Width Half Maximum (FWHM) of the Gaussian can be computed over the two axes of the image plane as a function of the variance through Equation 4.14.

$$\text{FWHM}_a = 2\sqrt{2\log 2}\sigma_a \approx 2.355\sigma_a \tag{4.14}$$

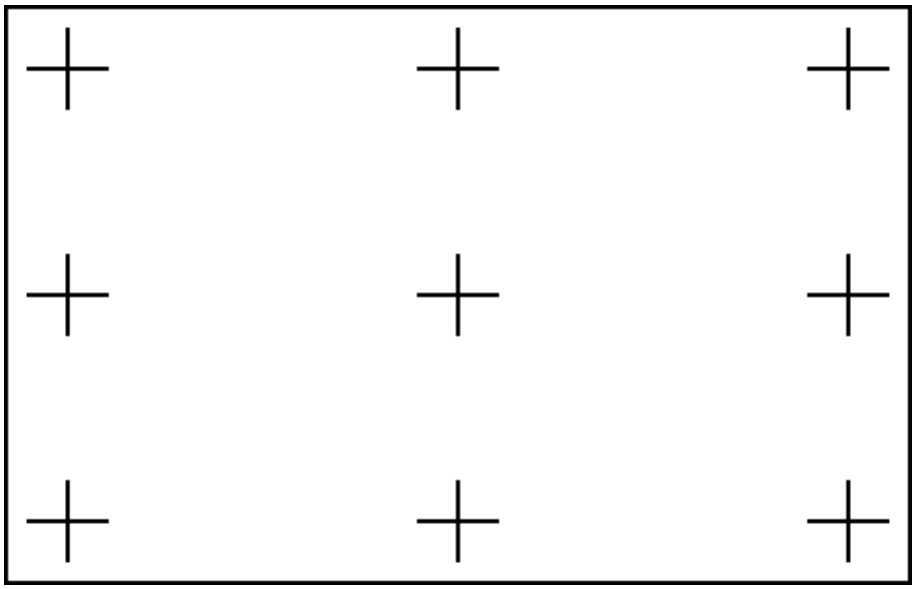

Figure 4.6: The cross symbols mark the spots to place the retro-illuminated hole.

Where $a \in \{x, y\}$ is the axis over the image plane; $\sigma_x = \Sigma_{0,0}$ and $\sigma_y = \Sigma_{1,1}$. The FWHM in pixels affects the actual linear resolution LR_a^{real} of the camera over the axis a as in Equation 4.15.

$$\mathrm{LR}_a^{real} = \mathrm{LR}_a^{estimated} \cdot \mathrm{FWHM}_a \tag{4.15}$$

4.7 Step 6: Detection Performance Testing

At the end of the *workflow*, all the main calibrations and characterisations of the chosen camera have been performed. It is now possible to digitally correct the photos into images that are, in principle, reliable from both the radiometric and geometric points of view. This final test step is required to verify whether the expected performance is indeed achievable in a laboratory twin of the actual deployment environment. One huge advantage of employing cameras is that optical images are scale-invariant. That is to say, the same scene at different scales is captured as the same photo if the ratios between the distances and the size of the objects are preserved. This trick enables ground simulation of sidereal distances in ground laboratories, where it would be impossible to separate the sensor and the target by hundreds of kilometres. Referring to Chapter 4.1, to simulate the dark LEO environment, it is required to employ the following assets: a *dark room*, a *dark background*, a light source, and a 2D or 3D miniature of the target in scale. Different from the actual space, a *dark room* still has physical boundaries, and light can bounce over the walls, creating an unrealistic diffuse flux and light incidence on the target's surface. That is why it is suggested to have as black as possible inner walls, absorbing visible light across internal bounces. This restriction becomes even more severe for the background of the target, as it is the baseline intensity above which the detection will be estimated. For such a reason, it is strongly recommended to employ a professional low-reflection surface as a *dark background*.

Two simple setups are illustrated by Figure 4.7:

- **Dark Room Facility**: with the availability of a voluminous facility with dark walls, it is possible to set up a larger dark background to avoid having undesired surfaces in the camera's FOV. Mechanical supports shall be planted to keep the camera and the uniform

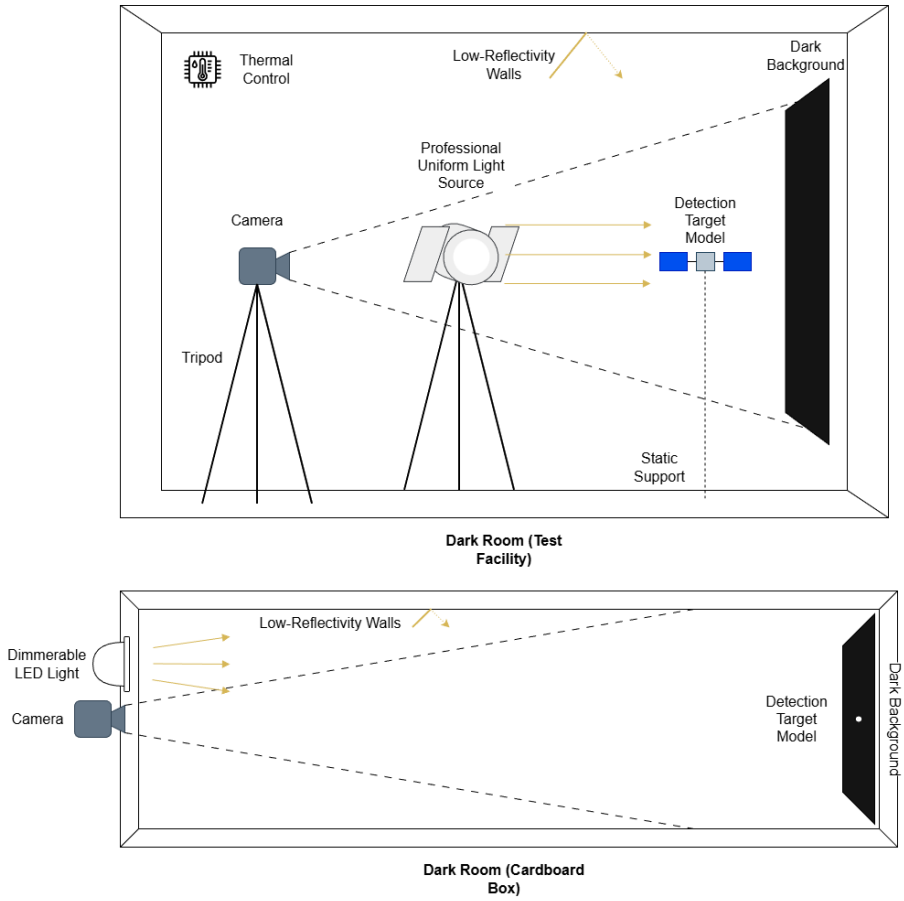

Figure 4.7: Dark Room Setup in both Test Facilities and Cardboard Box Simulations.

light source stable and still. By using a professional tripod, it is also possible to precisely calibrate the orientation of both, so as to accurately study different geometrical configurations, and possibly, streak scenarios. The detection model may be a miniaturised 3D version of the actual target with realistic paint reflectivity, and shall be stabilised by a thin or dark support. A dark background shall be placed in the back of the miniature to cover the whole frame, and can even be substituted with other surfaces simulating Earth's visible albedo. Temperature and humidity control can be implemented to cover and test different thermal noise levels;

- **Cardboard Box**: an easily accessible dark room can be implemented as a Cardboard Box, with a typically tenth of a centimetre long edge. The camera and the light can be placed on top of the box and fitted through designated holes, pointing toward the target. Given the tightness of the space, a narrow light beam is preferred to avoid too many bounces between the cardboard box walls. Finally, a dark background is laid down over the bottom of the box, with a micro-metric target on top of it, such as a microsphere or a paper cut-out. Typically, because of the reduced size and manoeuvrability of the miniature, there are limits on the testability of surface reflection and illumination angles with respect to the case of a high-end facility.

In summary, once the setup of the LEO orbit's reproduction is complete, multiple tests shall be performed by taking photos of the target with the chosen camera, in all the critical geometric configurations of interest among the ones mentioned in Chapter 3. The received intensity values shall be integrated, and the SNR of the reflection computed according to the formulas proposed in [35], eventually validating the error with respect to the theoretical estimation obtained in Step 1 (described in Section 4.2).

$$\text{SNR} = \frac{F}{\sqrt{F+B}} \tag{4.16}$$

Where F is the measured integrated flux over the PSF pixels; B is the integrated background noise over the PSF pixels based on background pixel estimations. If the target is visible at a given configuration and under a given light, it shall also be detectable on scale in its proper size at larger distances. Without accessing the actual deployment environment, this is a close-enough accessible approximation of the real scene for prototypical applications.

Finally, take into consideration the following recommendations:

- The cleaner the *dark room*, the better the performance. Dust which flies around and settles over the dark background can reflect visible light. This is particularly true in the Cardboard Box case, where the micro-metric targets' size is closer to the size scales of the dust;
- Use a radiometer to validate the illumination. Light flux can greatly change, particularly when the source is not designed for uniform illumination. Carefully fix the position and intensity of the light and account for hardly avoidable error margins;
- Carefully handle the *dark background*. Professional black sheets, in particular, are made of fragile fabrics which require attention and may even be degraded by contact with human skin. Above all, keep it properly clean from dust, as it not only settles over it, but may remain trapped in the stitches of the fabric.
- Keep in mind that the measures will always be affected by a general diffused light caused by the Rayleigh scattering, which is unavoidable, unless the tests are performed in an actual insulated void.

Chapter 5

Workflow Implementation

The entire end-to-end *workflow* is experimentally applied to a sample COTS camera to introduce it from a more concrete perspective and to validate its effectiveness. As a starting point, a **Arducam 100fps Global Shutter Color USB Camera Board, 1MP OV9782 UVC Webcam Module with Low Distortion M12 Lens** is selected for the experiment. The choice is justified by its accessibility, cost-effectiveness, and user-friendly UVC interface, which is USB-based. Table 5.1 reports a summary of the most relevant sensor and optic specifications, also available at [41]. They follow some considerations:

- The camera has a medium-sized FOV, which is a good fit for basic initial detection and surveillance;
- While the Effective Focal Length (EFL) is fixed, the experiment must be accomplished by also keeping a fixed Back Focal Length (BFL). For this experiment, all the measurements have been conducted at distances in focus with respect to the chosen fixed optical configuration;
- The camera interfaces via UVC, through which it is not possible to retrieve the Raw CFA image. While the selection of a sensor provided with an interface capable of accessing the raw data shall always be favoured, this camera can be used to demonstrate the need for radiometric calibration on a more challenging non-linear CRF. In particular, between the available MJPG and YUY2 formats, YUY2 is necessarily chosen due to MJPG being a compressed format and introducing undesired artefacts in its lossy compression process;
- A plethora of properties can be adjusted through software, AMCap, in the case of this experiment. Each internal processing operation that can be subject to auto-adjustment, such as exposure, white balance, and gain control, shall be fixed to a predictable given value. In particular, gamma shall be set to zero whenever possible, which should exclude exponential processing of the pixels' intensity.

The configuration for this experiment is reported in Table 5.2. This implies the camera has been configured to produce greyscale uncompressed bitmap images.

Let us assume that the choice of the camera was not decided with the experiment in mind, but that it is a potential candidate COTS to validate with respect to the desired detection requirements before the acquisition. Consider the minimum exposure allowed by the camera $\tau = 976.6\mu s$, a reasonable 3×3 PSF, typical CMOS noise ($\sigma_{\text{rd}} = 40e^-, \sigma_{\text{bg}} = 8666\frac{e^-}{s}$) [42], ideal optical efficiency $Q_{\text{opt}} = 1$, typical CMOS quantum efficiency $Q_{\text{eff}} = 0.4$ [42], and a minimum acceptable $\text{SNR}_{min} = 3$ [35]. Finally, assume a target reflectivity $\rho = 80\%$ in the visible that is approximately the same as the miniaturised target chosen for the experiment.

Property	Value
Sensor	$1/4''$ OV9782
Pixel pitch	$3\mu m \times 3\mu m$
Resolution	1 1MP 1280×800
Data Format	MJPG/YUY2
Frame Rate	MJPG 100fps@1280 x 800/720p/800 x 600/640 x 480/320 x 240; YUY2 10fps@1280 x 800/1280 x 720.
FOV	$70°$ (H)
Lens Mount	M12
Optical Format	$1/2.7''$
EFL	$2.8mm$
BFL	$2.6mm$
f/N	2.8
Spectrum	Sensitive to Visible Light
Power Supply	USB powered $5V$
Working Current	MAX $200mA$
Operating Temperature	$-20°C \sim +70°C$

Table 5.1: Specifications for OV9782 1MP UVC Webcam Module with Low Distortion M12 Lens.

Property	Value
Brightness	0
Constrast	32
Hue	0
Saturation	0
Sharpness	0
Gamma	100
White Balance	6500
Backlight Comp	0
Gain	0
Exposure	Fixed Accordingly
Compression	YUY2
Video Compressor	None

Table 5.2: Camera Acquisition and Processing Parameters Configuration.

All the formal computations presented in Section 4.2 are performed, and a $m_{\text{lim}} \approx -3.46$ is estimated. The following plots are illustrated:

- Figure 5.1 shows the AVM of the target vs. its distance. Estimates predict the sensor's ability to detect a $1m$-radius target at maximum $\sim 17km$. A good theoretical starting point for a cheap micro-camera. It is worth noting how the quadratic scaling with the distance and the target area becomes linear on a logarithmic scale;
- Figure 5.2 shows the AVM of the target vs. the phase angle, provided a given AVM cutoff. The AVM rapidly increases for high angles, which means less reflected light. Keep in mind

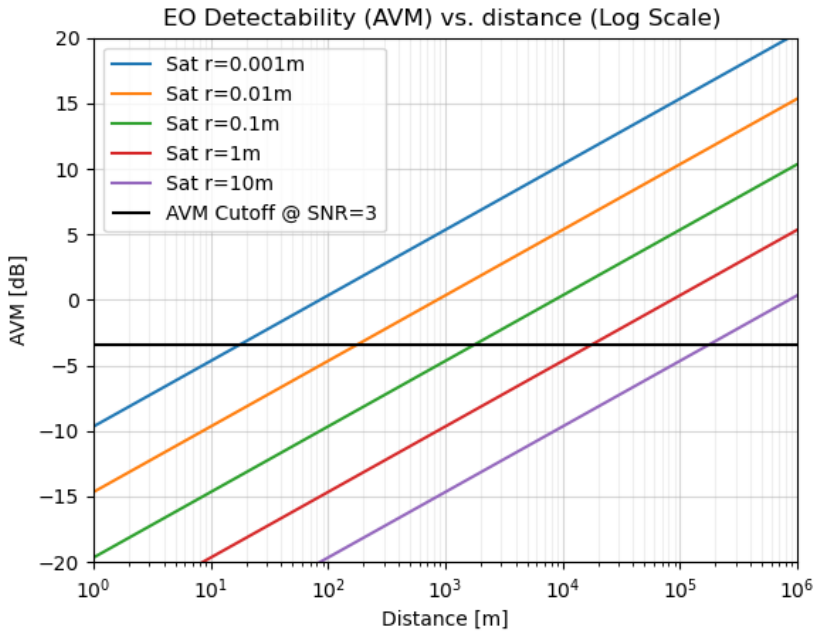

Figure 5.1: EO Detectability (dB) vs. Distance (m) for satellites with $r \in [1mm, 10m]$, at $m_{\text{lim}} = -3.46dB$ (SNR$_{min} = 3$) and $\phi = 0°$.

that a lower AVM value on a negative star magnitude scale means higher intensity;

- Figure 5.3 shows the maximum detectable distance vs. the phase angle. The curve rapidly falls for high phase angles;
- Figure 5.4 shows the Percentage Detection Range vs. the phase angle. A soft curve that is almost linear in the midrange;
- Figure 5.5 shows the Resolution vs. Distance. As expected, the performance is detector limited, with a linear resolution $PSSD_x = 1m$ at $1km$;
- Figure 5.6 shows the Maximum Streak Speed vs. Distance. The sensor shall be able to measure relative speeds parallel to the object plane up to $S^x_{max} \approx 1700\frac{km}{s}$ at $1km$, far above the average LEO orbit speed of $7.8\frac{km}{s}$.

Let us assume the result of the formal analysis is satisfying, and the estimated sensor's estimate fulfils the requirements for our space surveillance capability. Now, it is necessary to perform the geometric calibration of the camera. A large set of 63 calibration photos in a wide range of tridimensional orientations, well-illuminated, in-focus distances from the camera, and regions in the frame is used, with a substantial margin from the minimum required in terms of number of images. Figure 5.7 illustrates the statistical distribution of the re-projection error. A very dense bell centred in ~ 0.35 pixels can be easily distinguished, with a second peak nearby ~ 0.5 addressable to pictures more challenging in terms of pattern position and orientation in the frame. More in detail, Figure 5.8 reports how the re-projection error in pixels changes with respect to the centrality of the chessboard in the frame. This former proposed metric is measured as the average distance in pixels from the centre of the frame over all the vertices of the chessboard. As is more evident in plot (b), the re-projection error and its variance increases with the marginality of the pattern in the photos. Those results highlight an expected higher degradation near the borders. Although performance is considered acceptable for experimental purposes, it is worth noting that the error is dangerously close to 0.5 pixel, potentially causing unwanted projection errors on neighbouring pixels. For completeness, Table 5.1 reports the coefficients of

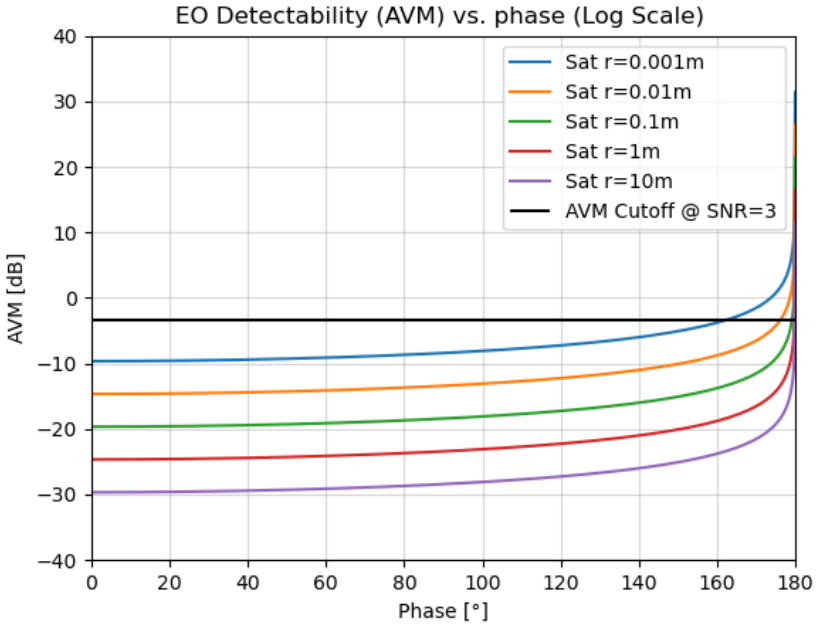

Figure 5.2: EO Detectability (dB) vs. Phase ($degs$) for satellites with $r \in [1mm, 10m]$, at $m_{\text{lim}} = -3.46dB$ ($\text{SNR}_{min} = 3$) and $R = 1m$.

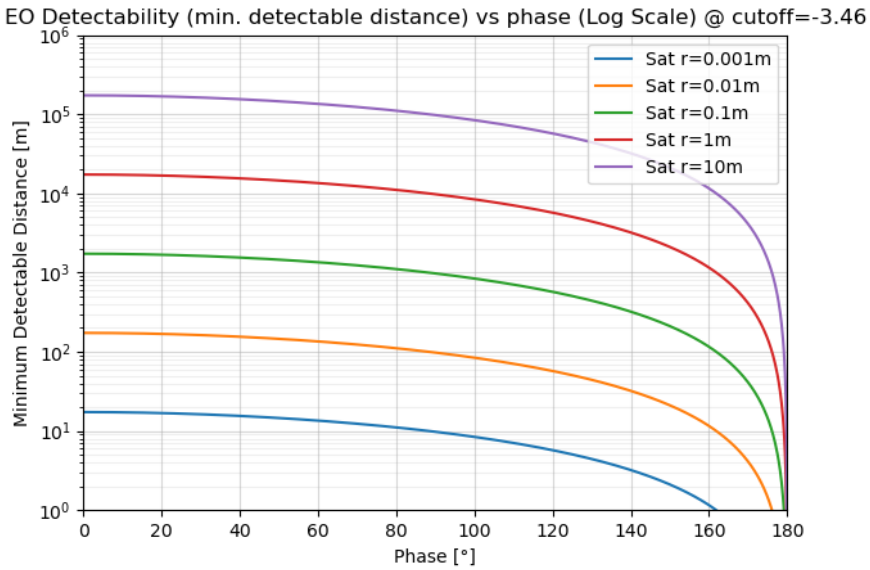

Figure 5.3: Minimum Detectable Distance (m) vs. Phase ($degs$) for satellites with $r \in [1mm, 10m]$, at $m_{\text{lim}} = -3.46dB$ ($\text{SNR}_{min} = 3$).

the intrinsic matrix **K**, which are compatible with the camera specifications and report no shearing. The implementation of the calibration algorithm provided by `OpenCV-python` also finds a vector of distortion coefficients **D** and uses a non-linear model to automatically fix possible lens effects. The values found for such vectors' components are reported in Equation 5.2, and the coefficients confirm the property of the camera of being low-distortion, according to its specifications.

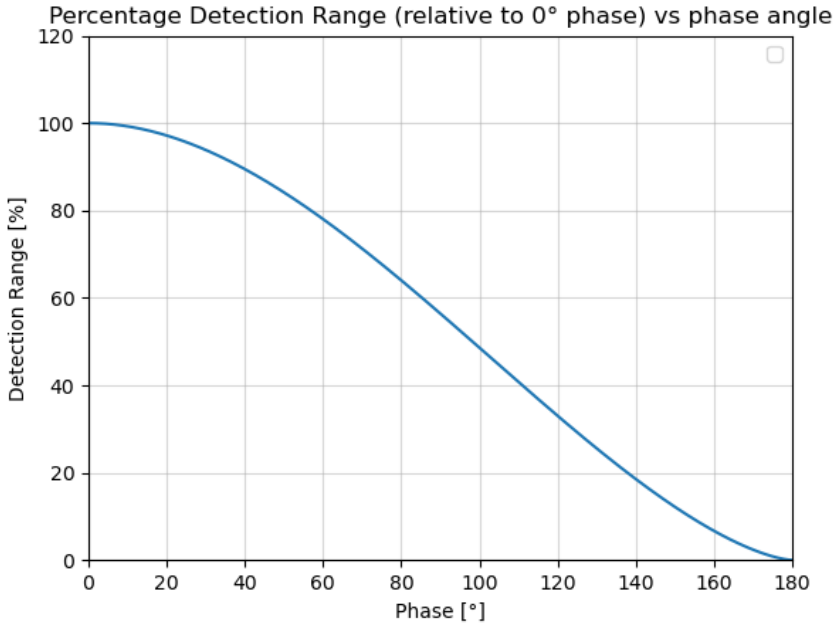

Figure 5.4: Percentage Detection Range relative to $\phi = 0°$(%) vs. Phase ($degs$).

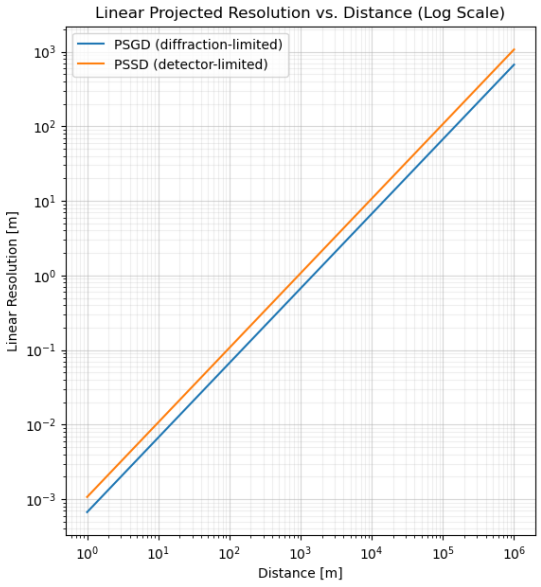

Figure 5.5: Diffraction and detection limited Resolution (m) vs. Distance (m).

$$\mathbf{K} = \begin{bmatrix} 898.32 & 0 & 682.57 \\ 0 & 898.80 & 407.87 \\ 0 & 0 & 1 \end{bmatrix} \tag{5.1}$$

$$\mathbf{D} = [0.0297, -0.0710, 0.0005, -0.0000, 0.0300] \tag{5.2}$$

The calibration of the intrinsic and distortion parameters is mandatory for the rest of the

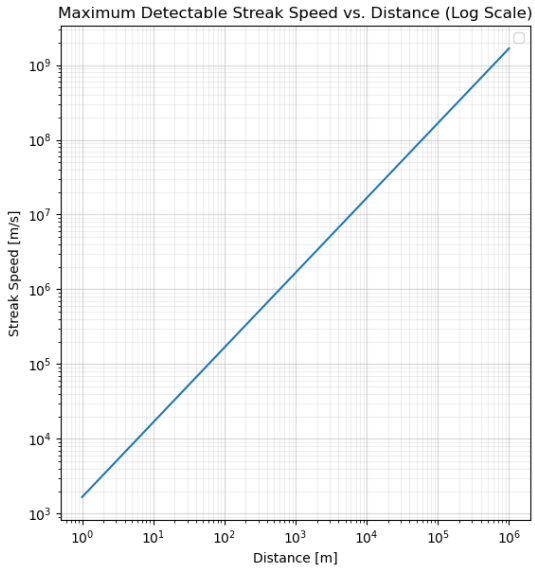

Figure 5.6: Max Detectable Streak Speed (m) vs. Distance (m).

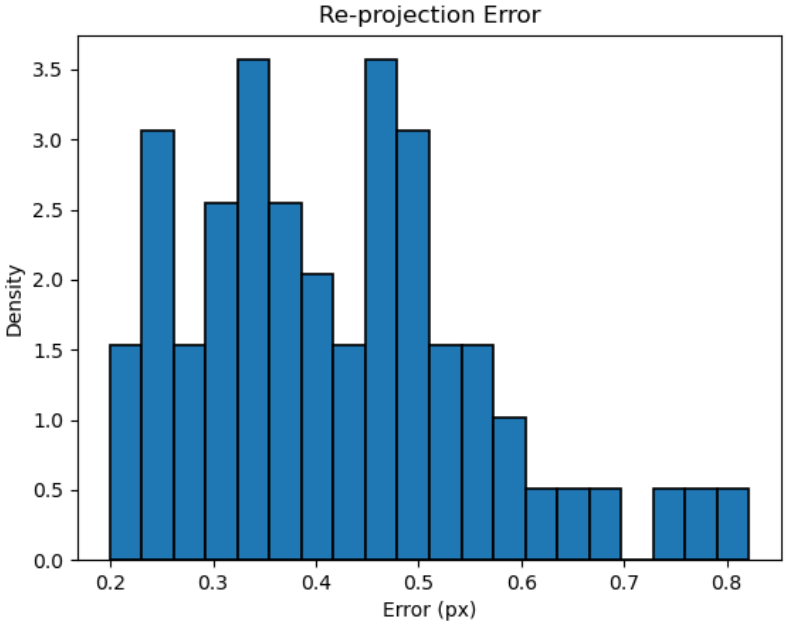

Figure 5.7: Re-projection Error Distribution.

workflow.

Once the calibration coefficients required for fixed camera distortion and projection errors are found, images for Radiometric Calibration can be acquired. Now, since the number of available options for the duration of the exposure τ is finite and small, one photo is taken for each value in the set $\{-10, -9, -8, ..., -4\}$, where the value is $\log_2$ of τ in seconds. Figure 5.9 shows the photo setup, which is fixed across different exposures. The photo is taken at a Macbeth chart, in particular a **Calibrite ColorChecker Classic Mini**, illuminated by a light whose uniformity is measured through a lux meter, whose specifications are reported in Table

(a) (b)

Figure 5.8: Re-projection Error Values (px) vs. Average Chessboard Points Distance from the centre (px) as a Scatter Plot (a) and histogram (b).

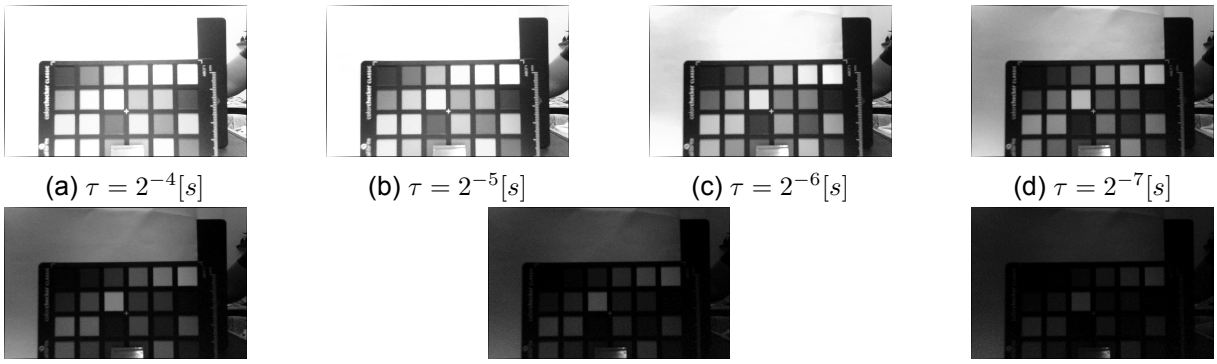

(a) $\tau = 2^{-4}[s]$ (b) $\tau = 2^{-5}[s]$ (c) $\tau = 2^{-6}[s]$ (d) $\tau = 2^{-7}[s]$

(e) $\tau = 2^{-8}[s]$ (f) $\tau = 2^{-9}[s]$ (g) $\tau = 2^{-10}[s]$

Figure 5.9: Example of photo for Radiometric Calibration taken at a Macbeth Chart at multiple different exposures.

Property	Value Range
Sensitivity Range	0–200,000 lux
Resolution (>1000)	1 lux
Resolution (<1000)	0.1 lux
Spectral Precision	CIE function $V(\lambda)$ ($f_1' \leq 6\%,\ f_2' \leq 2\%$)
Spectral Response	CIE photopic (human)
Sensor	Silicon photodiode with response filter

Table 5.3: Light Meter Specifications.

5.3. In particular, the calibration is conducted on a crop of the six greyscale patches in the first row of the ColorChecker, to avoid the impact of other lights. Finally, a crop for each of the patches is processed and stored for future examination.

For the inverse CRF calibration, the `OpenCV-python` implementation of the Debevec algorithm was used, configured with samples $N = 100$, $\lambda = 10$, and random sampling, where λ was tuned to the least value achieving monotonicity. The output radiance map g has been rescaled through a gain factor $G = \frac{244}{g(244)}$, to avoid normalising on saturated values, and clipped to avoid values out of the range $[0, 255]$. The desired output after applying the radiance map to invert the response is to have intensity values which scale linearly with the exposure, in coherence with physical laws. Figure 5.10 shows an exponential inverted CRF with clearly exponential growth. This implies that, despite the gamma being configured to 100 in AMCap ($\gamma = 1$) for linearity,

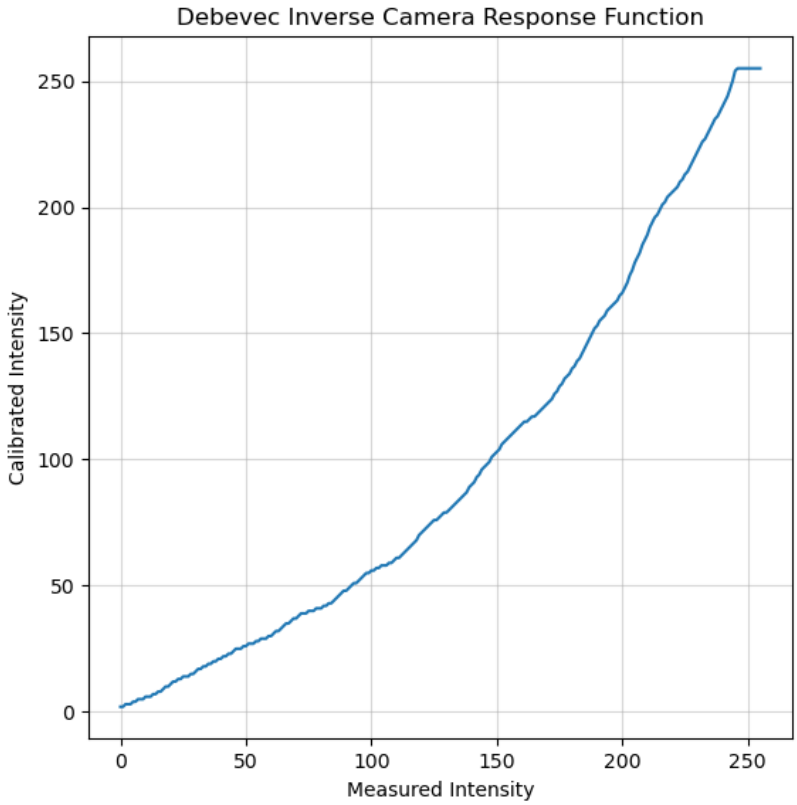

Figure 5.10: Inverted Camera Response Function computed through Debevec Algorithm.

there is an actual default coefficient to γ, which is usually $k = 2.2$ or $k = 0.45$. Although one could set an appropriate gamma value on the ISP directly, whether it is configurable, let us still optimise the radiance map to invert all the CRF contributions, assuming they are invariant across different frames. Now, the radiance map is applied as a look-up table to change the pixel intensity values and invert the response. Figure 5.11 illustrates both the original and linearised CRF curves' growth with the exposure time for all six greyscale patches of the Chart. The < 1 exponential decay of the original CRF is easily recognisable in the dotted curves, while the solid curve representing the linearised CRF values is approximately straight, as desired. Figure 5.12 shows the linear relationship, measured by the Pearson correlation, between pixel intensity and exposure for different reflectance coefficients. Figure 5.13 shows the correlation between pixel intensity and reflectivity for different exposures, which should also be linear according to radiative transfer equations. Saturated values are discarded for those measurements. As can be seen in Figure 5.12, the correlation score between intensity and exposure is high, pretty much for all the patches but for the highly reflective ones. This is probably due to the drop in saturated values, which are more present in brighter patches. On the other side, Figure 5.13 shows the correlation between the intensity and the reflectance drops at middle exposure values. Since the original CRF's non-linear curve had its maximum flexion at middle exposure values, this can be attributed to a larger error in larger corrections. Finally, an absolute correspondence between intensity values and light intensity has been measured with a small set of processed test images and the support of the light meter (Figure 5.14). For $\rho = 19.8\%$, the picture highlights the following equivalence: $64 = 64.8\text{lux} \cdot 2^{-7}s$, $127 = 64.8\text{lux} \cdot 2^{-6}s$, $108 = 109.7\text{lux} \cdot 2^{-7}s$, $240 = 293.3\text{lux} \cdot 2^{-7}s$, with a measured standard error of $\approx 7\%$ in the measure. Let us consider the approximation good enough in this context, and in consideration of the accessibility of the

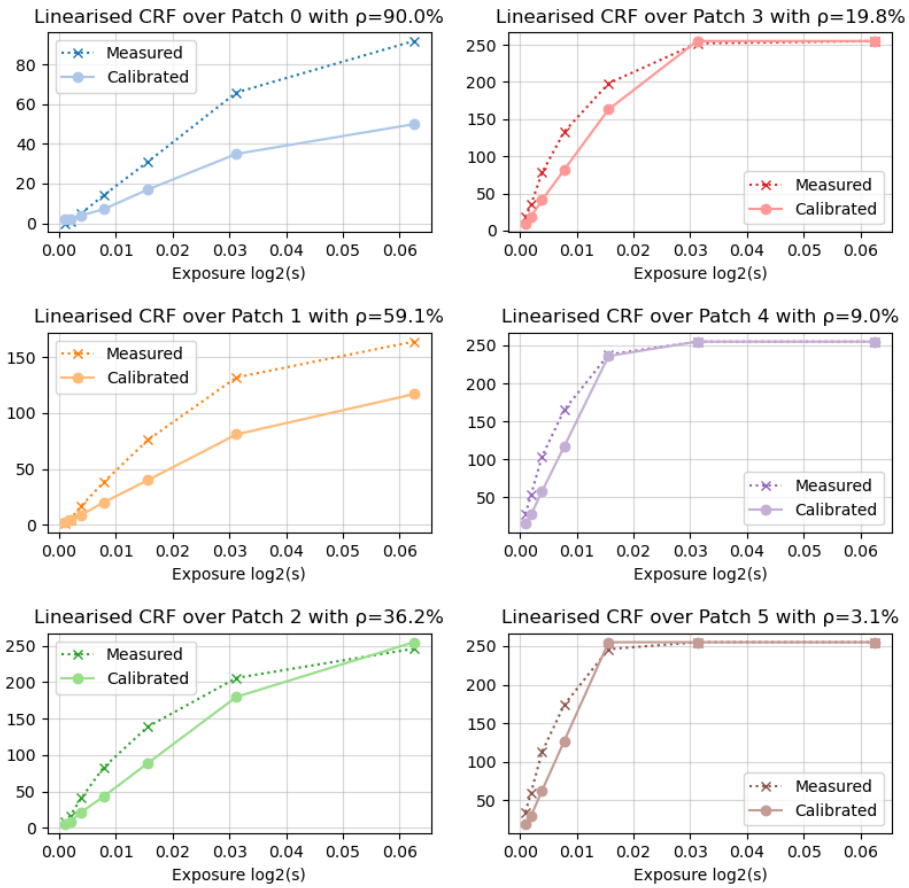

Figure 5.11: Linearised CRF vs. Exposures at different patches' reflectivities ρ.

camera; however, more meticulous calibration and test campaigns with larger test sets shall be conducted for an actual deployable system.

The next step is the error characterisation. At first visual glance, the camera is evidently affected by a strong dishomogeneous noise. Figure 5.15 is one frame of the video captured for the characterisation scenario, geometrically and radiometrically corrected by the previous processing steps. The choice of the location and illumination was, indeed, aimed to have a setup with almost all grey levels in $[0, 255]$ represented. However, Figure 5.16 clearly illustrates how the distribution is still dishomogeneous, even after the calibration steps. In particular, some grey levels are totally unrepresented, most probably due to the gamma correction, which introduces finer grain at low levels. In fact, the lower range is the only one where the expected monotonous increase of the error can be seen. Furthermore, interpolations from the geometric calibration introduce values in those missing range, with unreliable error values. The CRF inversion, as a pixel-wise transformation, not only cannot make up for this phenomenon, but more probably, being itself non-ideal, will introduce additional artefacts. This is why Figure 5.17 and 5.18, which illustrate the noise in a 2D and 3D fashion, respectively, appear to be so discontinuous. In cases like this, a more in-depth analysis can be performed with multiple scenes. However, such a further expansion of the calibration is not in the scope of this experiment. In addition, the dark signal noise is characterised in a video captured with the lens cap on, at the maximum exposure $\tau = 2^{-4}s$. As a result, the noise is approximately zero and will now be considered

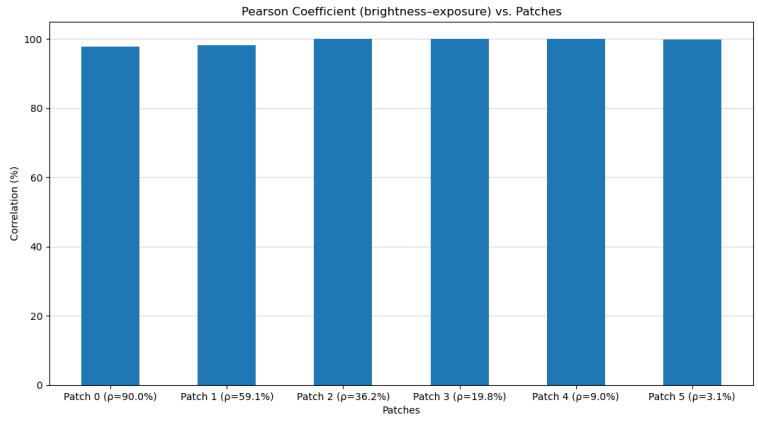

Figure 5.12: Correlation vs. Patch reflectivities ρ.

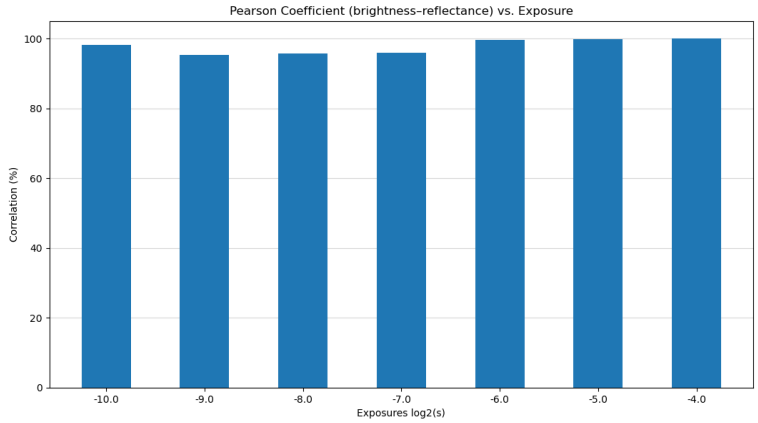

Figure 5.13: Correlation vs. Exposures.

negligible. Figure 5.19 illustrates an interesting normalised dark noise mask that shows a mild spot degradation of the signal in pixels at the lower angles of the frame corner.

As a last characterisation step, the geometric and the effective spatial resolution have to be computed. First of all, let us verify through an approximate setup the $PSSD$ value estimated through the initial formal analysis. The initial estimate for the geometric resolution was $1m$ at $1km$, a ratio of $1/1000$. Figure 5.20 shows a setup with a $5cm$-large metre located normally to the boresight at $70cm$ from the camera. The metre spans over $69px$ horizontally, which means a resolution of $\approx 0.7mm$ per pixel at $70cm$. The same ratio of $1/1000$ is obtained; let us consider this measure enough to confirm the $PSSD$ value in practice also for the vertical axis.

Now, let us proceed with the estimation of the PSF, which is required for the effective spatial resolution. To this aim, a micro-aperture is drilled in an aluminium plate to be retro-illuminated by a centred dimmable LED. Imperfections that may obstruct the hole and create circular PSF are removed with the help of a tweezer. The intensity and the distance of the sheet are manually calibrated to avoid saturated and off-focus pictures. One picture for each of the nine main configurations is taken according to Figure 4.6, as close as possible to the corners for the eight marginal positions. As mentioned in Section 4.6, the PSF is expected to be spatially varying, becoming narrower near the image centre and broader towards the periphery, with an elongation oriented radially outward.

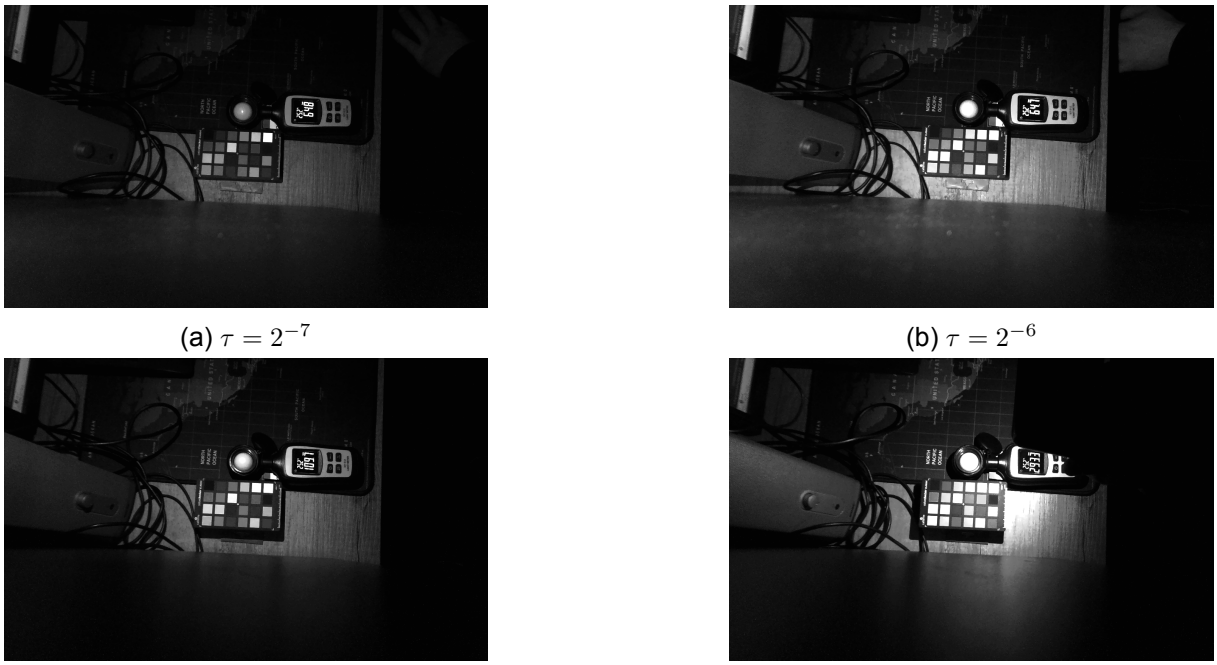

(a) $\tau = 2^{-7}$ (b) $\tau = 2^{-6}$

(c) $\tau = 2^{-7}$ (d) $\tau = 2^{-7}$

Figure 5.14: Test images for absolute flux values calibration and testing.

Figure 5.15: A frame from the video of the scene used in Noise Characterisation.

Figure 5.21 provides a side-by-side contrast-enhanced view of the actual photographed PSFs. According to the procedure introduced in Section 4.6, a Gaussian model is fitted over the PSF pictures to find the FWHM for both the axes x and y through a L-BFGS-B optimisation algorithm. Figure 5.22 reports the shape of the fitted distribution while Table 5.4 provides a tabular view. The estimated values are compatible with the typical predicted behaviour of a camera. The central PSF has, in fact, a FWHM ≈ 1.7 for both axes, which means that most of the energy is typically included in a 3×3 kernel. On the other side, we see a stretch on marginal PSF, particularly critical in the angles of the frame, where both the axes are stretched in a diagonal direction, with kernel edges up to 5 pixel long. Horizontally lateral PSFs are more dispersed than vertical ones, as that is the axis where the camera has the largest resolution,

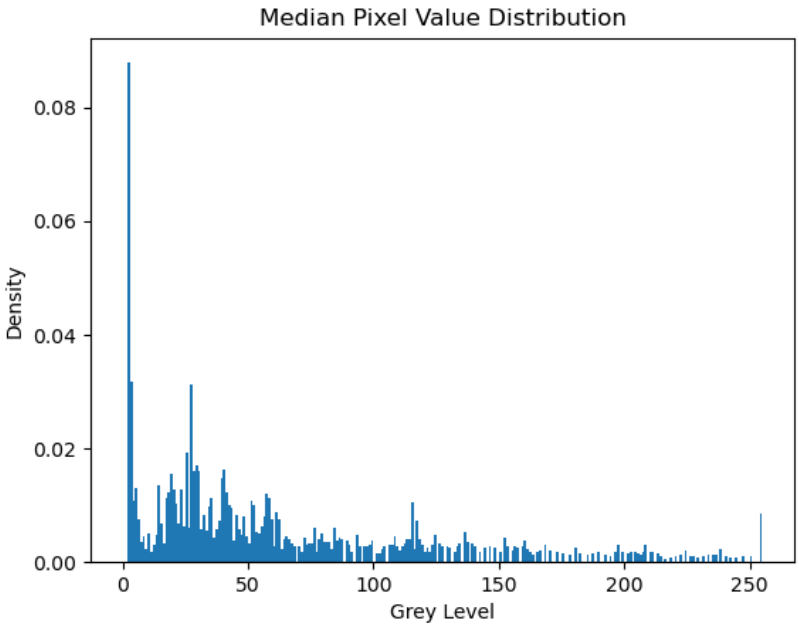

Figure 5.16: Grey levels density.

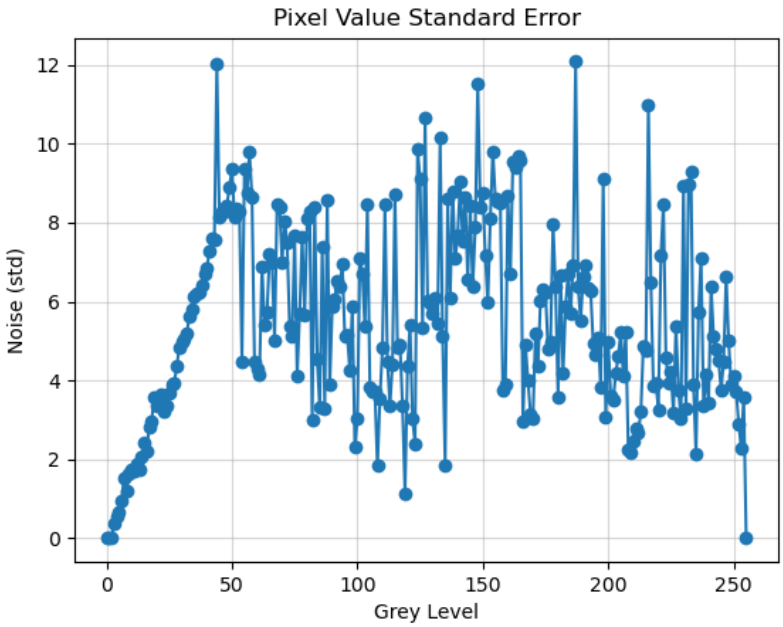

Figure 5.17: Noise Standard Error vs Grey Level.

and thus the PSFs are more distant from the centre. For this experiment, we will focus on an ideally centred target, compatible with a 3×3 disk, and a $\sim 1.7m$ spatial resolution at $1km$.

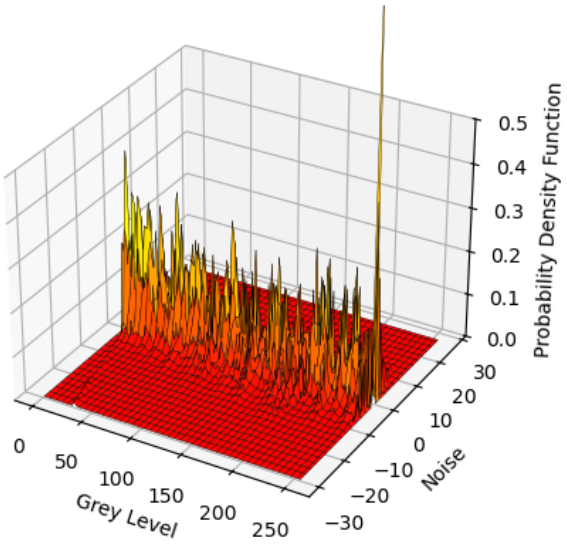

Figure 5.18: Noise Distribution vs Grey Level.

Figure 5.19: Normalised Dark Noise Mask.

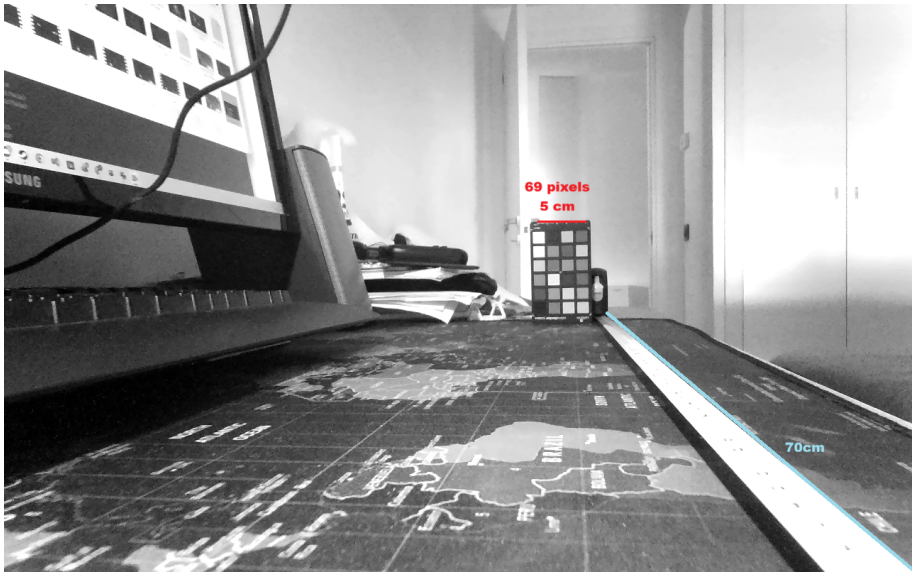

Figure 5.20: Picture taken at a Reference Metre ($5cm$) at a sample distance $70cm$.

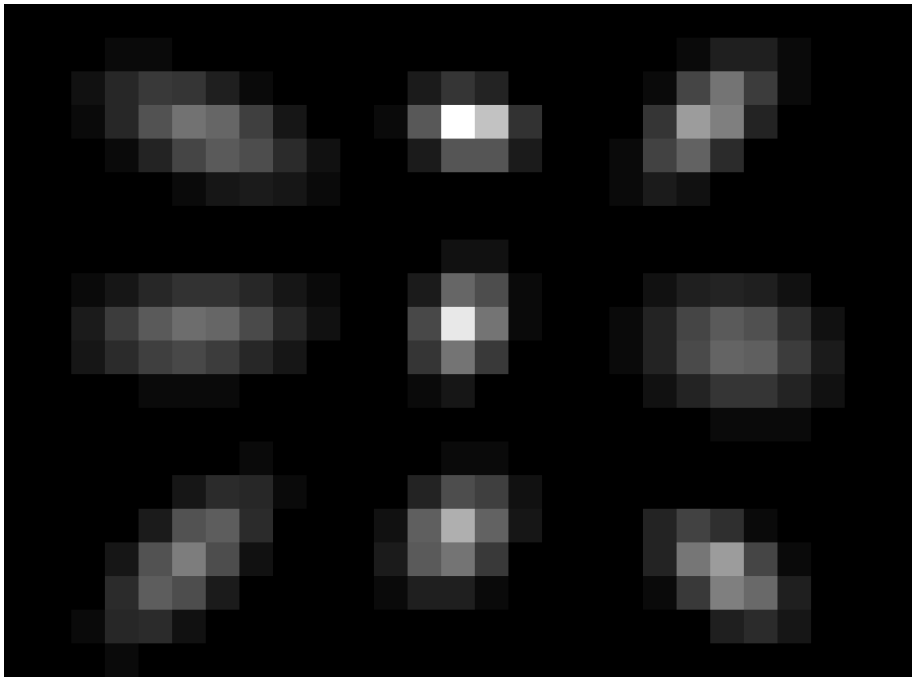

Figure 5.21: Summarised view of the PSF over the retro-illuminated hole at all the main regions in the frame.

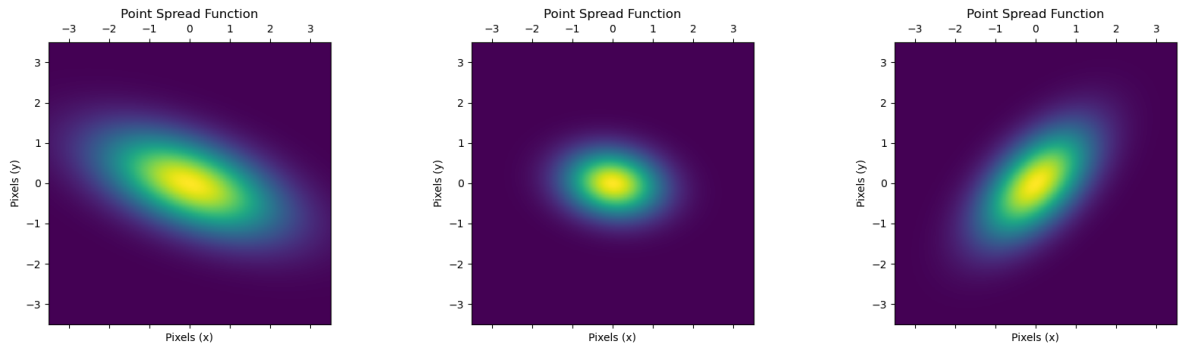

(a) Up – Left (b) Up (c) Up – Right

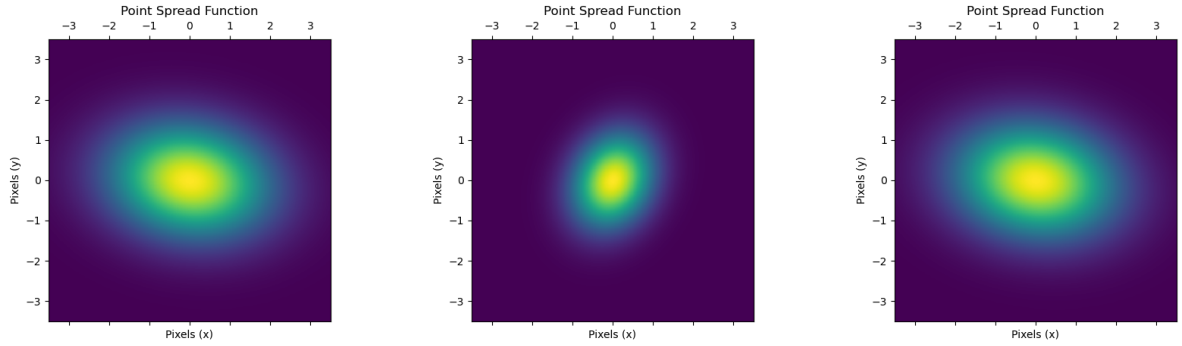

(d) Left (e) Centre (f) Right

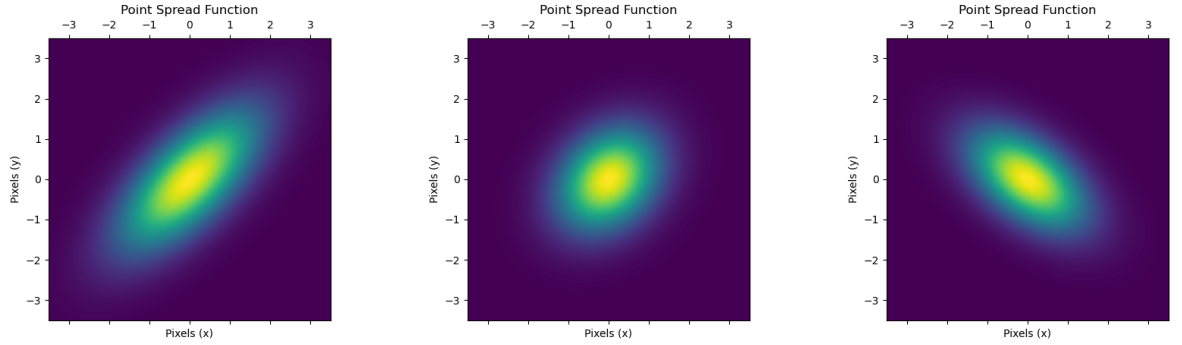

(g) Down – Left (h) Down (i) Down – Right

Figure 5.22: Bidimensional Discrete Gaussian models fitted over the Point Spread Function.

Position	FWHM$_x[px]$	FWHM$_y[px]$
Up–Left	3.52	2.03
Up	1.92	1.32
Up–Right	2.20	2.20
Left	3.89	1.78
Centre	1.62	1.87
Right	3.21	3.27
Down–Left	2.77	2.77
Down	2.03	2.03
Down–Right	2.30	1.99

Table 5.4: Point Spread Function Full-Width Half Maximum at x and y.

Chapter 6

Workflow Validation

Building a laboratory twin of the operative scenario is the most straightforward approach to validate the *workflow* and its results and predictions. For simplicity, let us focus on a simple case study, where the satellite target lies roughly at the centre of the camera, where the highest detection performance can be achieved. This simulation used a home-made Cardboard Box *dark room* of size $30 \times 30 \times 50cm$, covered with black cardboard internally. As a *dark background*, a Musou Black A4 fabric with absorptivity 99.905% is deposited on the floor of the box, and an A4 paper cut-out, approximated as a square with edges $\sim 500\mu m$ located in the centre of the FOV, at $50cm$ from the camera. Consider an approximated reflectivity of $\rho = 80$% [43] in the visible light spectrum. According to the camera's resolution, the paper cut should appear as a PSF. For the illumination, a digitally-controlled class-A GU10 Dimmerable Natural Cold White (6500K) LED 4.5W (50W equivalent) circular spotlight with 38 degrees beam is selected. Two circular apertures are cut on the top box flaps where the camera and the LED had to be fit to point down, toward the bottom, as in Figure 4.7, but rotated 90° clockwise. This represents an ideal 0 degree sun phase angle. Figure 6.1 shows the setup, with a miniature target enlarged for visualization purposes. In such a setup, four photos are taken at 100%, 80%, 60%, 50% of the LED's maximum intensity. However, the selected LED's behaviour seems not very linear with the intensity configured through the dimmer. Also, its emitted flux value is measured with an error of 10%. Furthermore, particularly in a home-made setup, such values can vary hugely with respect to the pointing direction of the light, the camera, and the non-ideal behaviour of the LED. In this case, let us consider this approximation good enough. Figure 4.7 shows the photo under the maximum light intensity. The difference in reflection between the dark board and the black cardboard of the box bottom is clearly visible. Also, a dim yet brighter than background disk appears at the centre of the dark background as a PSF. For each picture, that entire region of interest is cropped, and the SNR is computed with respect to the measured dark noise rather than the actual non-ideal background. Table 6.1 reports the SNR computed for the presented scene, and a formally Estimated Detection Distance (EDD) computed over the same scenario's conditions through the computation introduced in Section 4.2. The estimated

Light Flux $[\frac{W}{m^2}]$	SNR	EDD $[cm]$
~ 340	33.5	42
~ 300	18.5	66
~ 195	8.5	89
~ 140	3	150

Table 6.1: SNR computed under different illumination conditions and EDD for the scenario.

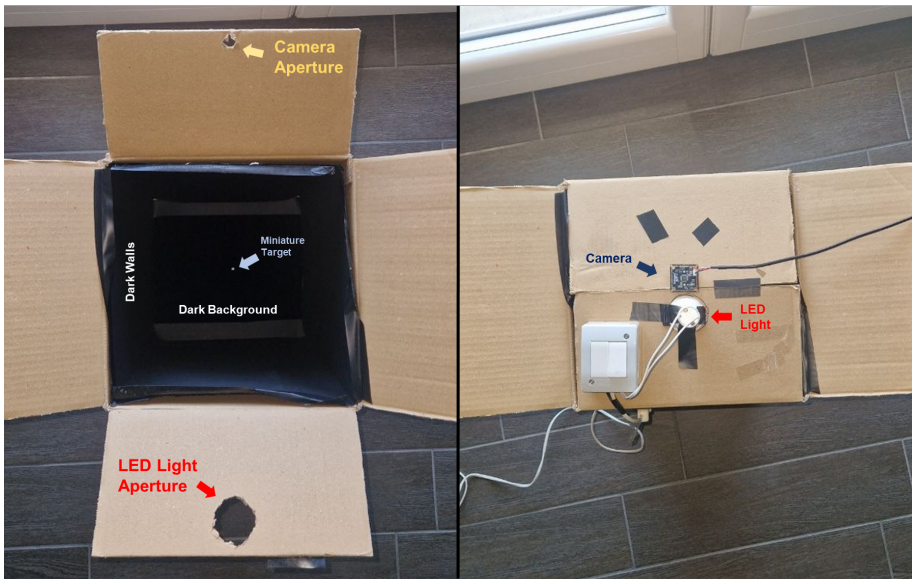

Figure 6.1: Experimental Cardboard Box Dark Room Setup (miniature over-size).

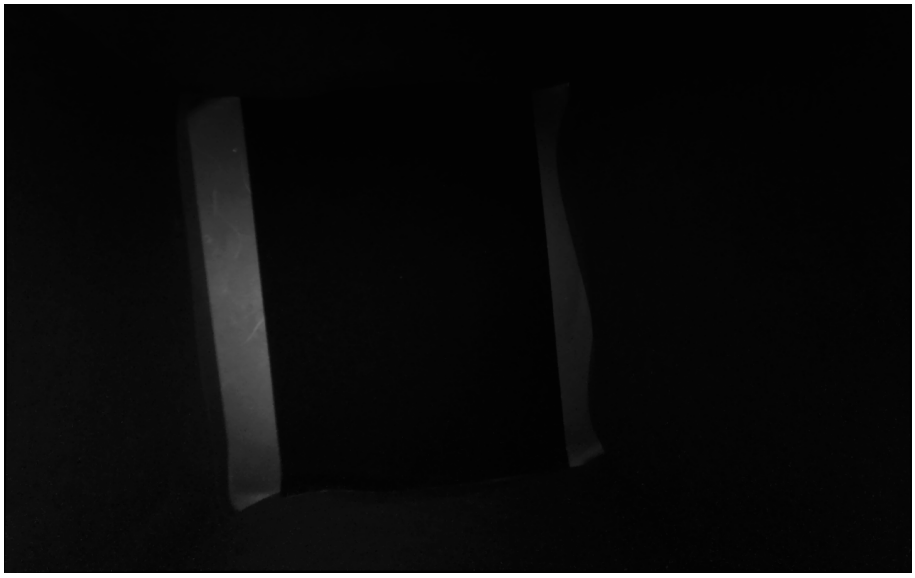

Figure 6.2: Photo Taken in the Dark Room setup with 100% intensity of the dimmer ($\sim 135W$).

detection distance values appear to have roughly the same magnitude order as the actual $50cm$ distance. Despite the encouraging preliminary approximate estimation, a concrete validation of the formal computations shall require a more systematic analysis, which development is out of the scope of this work, aiming to introduce the test procedure for the detection in a *dark room* under the available conditions.

Chapter 7

Conclusion and Future Works

In conclusion, the presented work explored the field of space-to-space SSA in LEO orbit. In particular, it focused on the emerging need of both national, international, and private organisations to protect their space assets from non-cooperative orbital threats. While most of the literature focuses on improving SSA against debris, the presented task has different constraints, which call for a multi-sensor solution. Among all the sensors, cameras stood out as the most promising starting point thanks to their passive power-effective way of detecting objects in the visible spectrum, and the advanced state of the art achieved in other consumer fields. A simple complete *workflow* was proposed to help the engineers in the selection of a proper camera through formal estimation of its performance, and to support its calibration and testing. A laboratory twin of the LEO environment was also proposed, along with practical instructions for its setup. Eventually, the workflow was implemented for a sample COTS camera in order to show its application with a practical example procedure and to validate its effectiveness. Despite the results being estimated with large error margins, due to the low-end resources, this work stands out as an entry point for whom is interested in approaching the quantitative imaging world. Calibration steps like in the proposed *workflow* are mandatory for any camera scientific application.

As a further development of this work, more accurate implementations of such *workflow* shall be implemented for cameras that are better suited for space applications. A better theoretical characterisation of the space environment can be performed, and solutions can be researched for currently unaccounted limitations. Furthermore, a more complete and detailed validation of the steps, in particular the detection performance formal estimation, can be conducted to accrete the reliability of the experimental results. This should include an operational test in the actual LEO orbit environment as definitive proof of its applicability. It is also worth exploring the possibility of extending this work to include infra-red cameras in the *workflow*, which have the potential to extend the use of optical sensors even in eclipse.

List of Tables

List of Figures

Bibliography

[1] *Navisp - design of crpas for aviation and high-accuracy services*. [Online]. Available: https://navisp.esa.int/opportunity/details/139/show.

[2] S. Egeli, "Space-to-space warfare and proximity operations: The impact on nuclear command, control, and communications and strategic stability," *Journal for Peace and Nuclear Disarmament*, vol. 4, no. 1, pp. 116–140, 2021.

[3] S. L. Montandon, "The element of surprise: Highly maneuverable satellites and ssa," *Journal of Strategic Security*, vol. 18, no. 3, p. 14, 2025.

[4] G. Mateo-Garcia et al., "In-orbit demonstration of a re-trainable machine learning payload for processing optical imagery," *Scientific Reports*, vol. 13, no. 1, p. 10 391, 2023.

[5] V. Vatsal, A. Kothandhapani, A. Subramanian, H. Vyas, and A. Jayaswal, "Challenges in onboard processing: Learnings from mission matterhorn," *arXiv preprint*, 2024.

[6] J. Ludwigson and A. Czyz, "Space situational awareness: Dod should evaluate how it can use commercial data," *United States Government Accountability Office*, 2023.

[7] K. F. Hussain, N. E.-D. Safwat, K. Thangavel, and R. Sabatini, "Space-based debris trajectory estimation using vision sensors and track-based data fusion techniques," *Acta Astronautica*, vol. 229, pp. 814–830, 2025.

[8] S. Hamidian, A. R. Kosari, and N. Assadian, "An optical space-based surveillance network for tracking leo debris," *IEEE Aerospace and Electronic Systems Magazine*, vol. 39, no. 10, pp. 18–35, 2024.

[9] M. Tagawa, T. Yanagisawa, H. Matsumoto, Y. Kitazawa, and T. Hanada, "A collaborative observation method based on a pair of space-based sensors and ground observatories for small debris in low earth orbit," *Transactions of the Japan Society for Aeronautical and Space Sciences, Aerospace Technology Japan*, vol. 12, no. ists29, Pr_27–Pr_34, 2014.

[10] A. Shtofenmakher and H. Balakrishnan, "Effects of phase angle and sensor properties on on-orbit debris detection using commercial star trackers," *Acta Astronautica*, vol. 221, pp. 318–330, 2024.

[11] A. Shtofenmakher and H. Balakrishnan, "Feasibility analysis of on-orbit debris detection using commercial star trackers," 2023.

[12] M. Liu, "Research on star sensor-based space debris detection and positioning technology," *Publications of the Astronomical Society of the Pacific*, vol. 135, no. 1046, p. 047 001, 2023.

[13] S. Dave, R. Clark, and R. S. Lee, "Rsonet: An image-processing framework for a dual-purpose star tracker as an opportunistic space surveillance sensor," *Sensors*, vol. 22, no. 15, p. 5688, 2022.

[14] D. Spiller et al., "On-orbit recognition of resident space objects by using star trackers," *Acta Astronautica*, vol. 177, pp. 478–496, 2020.

[15] M. Vernier, J. Lavigne, F. Grandmont, and S. Thibault, "Simulation of resident space objects detection from space-based optical imaging," in *Sensors and Systems for Space Applications XIII*, SPIE, vol. 11422, 2020, pp. 102–109.

[16] T. Flohrer, H. Krag, H. Klinkrad, and T. Schildknecht, “Feasibility of performing space surveillance tasks with a proposed space-based optical architecture,” *Advances in space research*, vol. 47, no. 6, pp. 1029–1042, 2011.
[17] C. Sun, Y. Sun, X. Yu, and Q. Fang, “Rapid detection and orbital parameters’ determination for fast-approaching non-cooperative target to the space station based on fly-around nano-satellite,” *Remote Sensing*, vol. 15, no. 5, p. 1213, 2023.
[18] R. Rosok, N. Bartels, W. Riede, M. Vogel, P. Wagner, and T. Dekorsy, “Method for improving the positional accuracy in passive optical detection of space objects,” *Applied Optics*, vol. 63, no. 18, pp. 4964–4973, 2024.
[19] W. Zhang and P. Hu, “Toward onboard ai-enabled solutions to space object detection for space sustainability,” *arXiv preprint arXiv:2505.01650*, 2025.
[20] M. Schubert, L. Böttcher, E. Gamper, P. Wagner, and E. Stoll, “Detectability of space debris objects in the infrared spectrum,” *Acta Astronautica*, vol. 195, pp. 41–51, 2022.
[21] Ö. Yılmaz, N. Aouf, E. Checa, L. Majewski, and M. Sanchez-Gestido, “Thermal analysis of space debris for infrared-based active debris removal,” *Proceedings of the Institution of Mechanical Engineers, Part G: Journal of Aerospace Engineering*, vol. 233, no. 3, pp. 811–822, 2019.
[22] S. Catsamas et al., “Thermal infrared characterization of spatially unresolved resident space objects: Prospects from analytical two-component modeling,” *Advances in Space Research*, 2025.
[23] M. Driedger, A. Asgari, and P. Ferguson, “Feasibility of gathering resident space object range measurements using in-orbit observers,” *IEEE Journal of Radio Frequency Identification*, vol. 6, pp. 250–257, 2022.
[24] I. Lopez-Calle, “Space debris in-orbit detection with commercial automotive lidar sensors,” *Sensors*, vol. 24, no. 22, p. 7293, 2024.
[25] R. Gao and L. Dong, “Analysis of constraints on the remote application of inverse synthetic aperture laser radar,” *Sensors*, vol. 24, no. 11, p. 3381, 2024.
[26] E. Marchetti, A. G. Stove, E. G. Hoare, M. Cherniakov, D. Blacknell, and M. Gashinova, “Space-based sub-thz isar for space situational awareness—concept and design,” *IEEE Transactions on Aerospace and Electronic Systems*, vol. 58, no. 3, pp. 1558–1573, 2021.
[27] G. Cohen et al., “Event-based sensing for space situational awareness,” *The Journal of the Astronautical Sciences*, vol. 66, no. 2, pp. 125–141, 2019.
[28] K. Xiao et al., “A preliminary research on space situational awareness based on event cameras,” in *2022 13th International Conference on Mechanical and Aerospace Engineering (ICMAE)*, IEEE, 2022, pp. 390–395.
[29] T. Haarlammert, A. Kwiatkowski, M. Möller, F. Kröber, U. Schmidt, and S. Chelkowski, “Threat detection, identification, and optical counter measures for space-based applications,” in *High-Power Lasers and Technologies for Optical Countermeasures*, SPIE, vol. 12273, 2022, pp. 33–48.
[30] M. Pajusalu et al., “Sispo: Space imaging simulator for proximity operations,” *PloS one*, vol. 17, no. 3, e0263882, 2022.
[31] H. Krüger, S. Theil, M. Sagliano, and S. Hartkopf, “On-ground testing optical navigation systems for exploration missions,” in *9th ESA Conference on Guidance, Navigation & Control Systems*, 2014.
[32] B. Boone, J. Bruzzi, W. Dellinger, B. Kluga, and K. Strobehn, “Optical simulator and testbed for spacecraft star tracker development,” in *Optical Modeling and Performance Predictions II*, SPIE, vol. 5867, 2005, pp. 318–331.
[33] *7x9 checkboard for camera calibration (20x20 mm) 1:1 on a4 paper*. [Online]. Available: https://www.mrpt.org/downloads/camera-calibration-checker-board_9x7.pdf.
[34] D. Pascale, “Rgb coordinates of the macbeth colorchecker,” *The BabelColor Company*, vol. 6, no. 6, 2006.

[35] A. Zakharov, M. Prokhorov, M. Tuchin, and A. Zhukov, “Minimum star tracker specifications required to achieve a given attitude accuracy,” *Astrophysical bulletin*, vol. 68, no. 4, pp. 481–493, 2013.

[36] Z. Zhang, “A flexible new technique for camera calibration,” *IEEE Transactions on pattern analysis and machine intelligence*, vol. 22, no. 11, pp. 1330–1334, 2000.

[37] *Opencv camera calibration tutorial in python*. [Online]. Available: https://docs.opencv.org/3.4/dc/dbb/tutorial_py_calibration.html.

[38] P. E. Debevec and J. Malik, “Recovering high dynamic range radiance maps from photographs,” in *Seminal Graphics Papers: Pushing the Boundaries, Volume 2*, 2023, pp. 643–652.

[39] A. Bevilacqua, A. Gherardi, and L. Carozza, “A robust approach to reconstruct experimentally the camera response function,” in *2008 First Workshops on Image Processing Theory, Tools and Applications*, IEEE, 2008, pp. 1–6.

[40] A. Bevilacqua, L. Di Stefano, and A. Lanza, “A simple self-calibration method to infer a non-parametric model of the imaging system noise,” in *2005 Seventh IEEE Workshops on Applications of Computer Vision (WACV/MOTION’05)-Volume 1*, IEEE, vol. 2, 2005, pp. 229–234.

[41] *Ov9782 global shutter color cameramodule*. [Online]. Available: https://core-electronics.com.au/attachments/localcontent/B0385_OV9782_Global_Shutter_UVC_Camera_Datasheet_19190316e78.pdf.

[42] B. A. Fowler, A. El Gamal, D. X. Yang, and H. Tian, “Method for estimating quantum efficiency for cmos image sensors,” in *Solid State Sensor Arrays: Development and Applications II*, SPIE, vol. 3301, 1998, pp. 178–185.

[43] R. Kumar, V. Kumar, and V. Sharma, “Discrimination of various paper types using diffuse reflectance ultraviolet–visible near-infrared (uv-vis-nir) spectroscopy: Forensic application to questioned documents,” *Applied spectroscopy*, vol. 69, no. 6, pp. 714–720, 2015.

Acknowledgments

This work marks the end of a year-long chapter of my journey in space science, and, hopefully, the beginning of a much longer one. Like many others, my passion for space exploration is deeply rooted in my childhood, and I hope my humble contribution will support science that inspires people to be curious, as I used to be when, as a child, I used to watch my beloved astronomy documentaries. However, it is extremely rare that one's achievements are only one's own, and this is no exception. In this regard, I want to thank all the people who contributed directly or indirectly to the realisation of this accomplishment.

I want to thank Professor Bevilacqua, my supervisor, as its support was invaluable. He led me patiently through the field of quantitative imaging, much deeper than I had during my career to date.

I want to thank my parents for their support in my studies and in life, and for their infinite patience and love. In particular, I would like to thank my dad, Luigi, whose passion for space and technology shaped mine and taught me the value of knowledge and curiosity more than anyone else.

I want to thank my beloved cousin, Stefano, who never misses the chance to lend me a hand when I call for help. As an academic, he is in an everlasting search for answers, both in work and life, and I hope we will continue to walk this path together, even on different routes.

I want to thank my family, my friends, and all the people who care for me, always supporting me, sharing with me both struggles, successes, and happy moments. I could not have done it without the serenity that they give me every day.

I want to thank all my colleagues and superiors at the ELT Group, who supported my career growth and choices regardless. They also gave me the chance to work on this stimulating, innovative thesis, hoped that it can be the baseline for our future technological innovations. I am deeply grateful for how they valorise my work every day.

I would like to thank anyone who showed interest in my studies and work, for they gave me the chance to share my knowledge and passion, which always brings me so much joy.

Finally, I would like to thank my loved ones who cared for me and believed in me, and who are no longer here to celebrate this achievement with me. I will never forget their love, and I owe who I am today to them; a debt I can never repay, except by carrying my fondest memories of them throughout my life journey.